[Project Report]

Date: May 30, 2022

New Exploratory Research (Project No.: 2021H-04)

To the Director of the Disaster Prevention Research Institute, Kyoto University,

Applicant (Principal Investigator)
Name: Chao Huang
Position: PhD Student
Affiliation: Graduate School of Science, Kyoto University

The results of the collaborative research are reported as follows.

Project title: Effect of fines on the initiation and movement mechanisms of fluidized landslides
Principal Investigator: Chao Huang
Affiliation: Graduate School of Science, Kyoto University
Name of DPRI CP (contact person): Gonghui WANG
Research period: 06.01, 2021 ~ 03.31, 2022
Research location: Research Center on Landslides (Laboratory: N-157D and S-116D)
Number of participants in the collaborative research: 5 (DPRI: 1 non-DPRI: 4)
- Number of graduate students: 4 (Masters: 1; Doctoral students: 3) (Included number)
- Participation role of graduate students [Experimental tests; Lab assistance; Data analysis; Discussion]

Anticipated impact on research and education

By now, most understanding of non-plastic fines effect has relied almost entirely on element testing of small specimens under idealized conditions, lack of landslide physical modeling experiments verification and physical mechanism research. This study provides valuable insights into post-failure behavior of fluidized landslides and then enhances understanding for catastrophic geohazards, which could provide information for understanding the whole progress hazard chain of landslide hazards.

Research report

(1) Purpose

This study aims at examining the effect of non-plastic fines content on the initiation and movement of rainfall-induced fluidized landslides.

(2) Summary of research progress

Sandy slope was made in a large-scale flume, and then landslides were triggered on the slope through

sparkling water from above. The sandy slope was made by different samples that are mixture of silica sand No. 7 with differing contents (0 %, 10 %, 20 %, 30 %, 40 %) of silica powder by weight. Different sensors for measuring the soil layer tilting, displacement and pore water pressure were installed at different locations of the soil slope. A camera was used to monitor the landsliding phenomena. On the other hand, ring shear tests were also conducted to examine the liquefaction potential of these materials with different contents of fines.

(3) Summary of research findings

The varying non-plastic fines content has a remarkable effect on the initiation and movement of rainfall-induced landslides when their relative densities are approximately the same. When the fines content on the sample is the same, the relative density shows significant effects on the landsliding behavior. Transformation from retrogressive landslide type to fluidized landslide type was clearly identified by tilt sensor and displacement sensor. Equivalent void ratio could be used to better explain the behavior of mixtures with fines. It is inferred that the addition of fine particles into coarser grains alters the internal contact microstructure of matrix. In the mixtures with fine content less than a possible threshold, the mechanical behavior is dominated by the coarser particles contact, fine grains have a secondary role in the transfer of inter-grain forces. However, once fines content exceeds the threshold, the behavior of mixtures is primarily affected by fine-grains contacts, and the role of coarser particles becomes less important.

(4) Publications of research findings

- Huang C, Wang G H. (11, 2021): Effect of non-plastic fines content on the initiation and movement of rainfall-induced fluidized landslides, サイエンス倶楽部デイ 2021, Kyoto Univ., Online
- Huang C, Wang G H. (2, 2022): On the Rainfall-induced Landsliding Behavior of Sandy Materials with Different Fine Particle Contents in Flume Tests, 2022 DPRI Annual Meeting, Kyoto Univ., D104

The main report is as follows.

Effect of fines on the initiation and movement mechanisms of fluidized landslides

1. Introduction

Rainfall-induced landslides pose significant natural hazards in most parts of the earth especially in mountainous areas, which could be characterized by an extensive range of motion patterns. Deadly rainfall occurred frequently with climate change, causing numerous landslides such as 1999 Hiroshima landslide (Wang et al., 2003), 2004 Tokushima landlside (Wang et al., 2005), Hiroshima landslides triggered by heavy rainfall on 25 July, 2009 (Tsuchida et al., 2014) and 20 August 2014 (Wang et al., 2015), which has resulted in the destructive damage and great loss of lives and properties. Among hazardous deadly rainfall triggered landslides, fluidized landslides show fluid-like motion (Spence and Guymer, 1997), which are characterized by high mobility and long runout distance. This kind of fluidized landslides were also been documented on other planetary in solar system including Mars, Venus and lapetus (Crosta et al., 2018; Lucas et al., 2014; Magnarini et al., 2019), indicating this kind of landslides are universal geomorphological phenomena.

Several experimental investigations and theoretical analyses have been carried out to study the initiation mechanism and motion of fluidized landslides including flume test, triaxial test and filed investigation (Castro and Poulos, 1977; Eckersley, 1990; Green and Ferguson, 1971; Hu et al., 2017; Ishihara, 1993; Iverson, 2000; Olivares and Damiano, 2007; Seed, 1968; Spence and Guymer, 1997; Tang et al., 2020; Wang and Sassa, 2003, 2001, 1998). Great attention has been given to the role of liquefaction behavior in the initiation and movement of landslides. Liquefaction is a progress that the soil mass loses a large proportion of shear resistance because of the generation of high pore water pressure, which could be induced by dynamic loading such as earthquakes (Ishihara, 1993; Seed, 1979) or static loading such as rainfall, snowmelt and ground water variation (Castro and Poulos, 1977). Undrained loading fundamental mechanism was proposed to explain the generation of excess pore-fluid pressure and movement of flows slides (Hutchinson, 1986; Hutchinson and Bhandari, 1971). A fluidization model was pointed out for landslide-triggered flow where undranied loading of moving sliding mass onto the saturated alluvial deposit and torrential deposit, which can produce high pore pressure (Sassa, 1998, 1988). Sassa et al. (1996) also illustrated sliding surface liquefaction mechanism for high excess pore water pressure production caused by grain crushing near slip surface with the progress of shearing. Most of understanding on liquefaction mechanism is based on element tests with small specimens under idealized and limited conditions.

Many scientists used landslide physical modeling with different scale on artificial/natural slopes or in situ field monitoring methods to study landslide behavior and debris flow progress (Beaulieu et al., 2021; Chang et al., 2021; Deng et al., 2019; Dufresne, 2012; Fang et al., 2022; Fukuzono, 1985; Harp et al., 1990; Hunger and Morgenstern, 1984; Iverson, 2015; Iverson et al., 2011; Keefer et al., 1987; Koyama et al., 2008; Kornei, 2019; Leroueil, 2001; Nagl et al., 2020; Ochiai et al., 2007; Oka, 1972; Olivares et al., 2018; Pajalić et al., 2021; Picarelli et al., 2008; Regmi et al., 2014; Saito, 1965; Sasahara, 2022; Sasahara et al., 2011, 1996; Sasahara and Sakai, 2017, 2014; Sun et al., 2021; Tanaka, 1956; Yagi et al., 1985, 1983; Yamaguchi et al., 1989; Yang et al., 2021; Yatabe et al., 1986). Flume test as an effective physical simulation method was used to simulate landslide motion, debris flow evolution and deposition, fluvial erosion, rock-ice avalanches, landslide dams failure and pyroclastic density currents (Arran et al., 2021; Baselt et al., 2022, 2021; Cogan and Gratchev, 2019; de Haas et al., 2015; Delannay et al., 2017; Farin et al., 2014; Haas et al., 2021; Lamb et al., 2015; K. Li et al., 2021a; Lourenço et al., 2006; Lube et al., 2019, 2015; Mangeney, 2011; Mangeney et al., 2010; Ng et al., 2022; Nicollier et al., 2021; Prancevic et al., 2014; Ren et al., 2021; Saletti and Hassan, 2020; Z. Sun et al., 2021; Vicari et al., 2022, 2021; Xu et al., 2022; Yang et al., 2019; Z. Zhang et al., 2020; Zheng et al., 2021; Zhou et al., 2022). In the flume tests, Eckersley (1990) induced flowslides in small coking coal stockoiles through raising water table, showing excess pore water pressures were generated during movement rather than before motion, thus, liquefaction resulted from shear failure rather the cause. Spence and Guymer (1997) conducted laboratory flowslide study on loose saturated fine quartz sand and analyzed the motion of sands and pore pressures during motion. Wang and Sassa (1998, 2003, 2001) studied initial soil porosity effect and sample thickness effect on the pore pressure build-up, showing there was an optimal density for pore pressure build-up, where the moving velocity and motion distance were greatest. Iverson et al. (2000) triggered experimental landslides by rising pore water pressure, the landslides moved at contrasting velocities due to small differences in initial porosity. Okura et al. (2002) and Take et al. (2014) highlighted different phases of soil slope collapse in landslide event, involving the localized generation of excess pore pressure caused by static liquefaction. Ochiai et al. (2004) conducted a rainfall-induced landslides test on the natural slope to reproduce a fluidized landslide at almost field scale to avoid scaling

problems and mimic nature. Moriwaki et al. (2004) performed a full-scale rainfall induced landslide experiment, the landslide initiated successfully and slip surface formation was documented, the results showed that increasing response of pore water pressures to the soil mass resulted from different mechanisms in different parts of slope. For landslide modeling tests, crackmeters or extensometers have been employed in landslide surface displacement and internal movement monitoring (Fukuzono, 1985; Intrieri et al., 2012; Smethurst et al., 2017; Zhang et al., 2020). Recently investigations on tiliting behavior and movement of the slope surface were carried out by performing landslide modeling and field test on a natural slope (Kamai and Shuzui, 1986; Putra et al., 2021; Sheikh et al., 2021; Uchimura et al., 2015, 2010; Wang et al., 2022; J. Xie et al., 2020; M. Xie et al., 2020). However, few attempts have been done on the inner tiliting behavior of soil mass on the slope failure (Iverson, 2000; Sasahara, 2022).

Although great efforts have been devoted to study initiation and movement of landslides, efforts are still needed to enhance the understanding of landslide process, particularly non-plastic fines effect. Fine particles exit in the landslide in abundance including original slope and landslide deposits. For original slope, some landslides with long traveling distances tend to occur on the materials rich in fine soil particles like granitic soil produced by weathered coarse-grained granite, such as the 2014 Hiroshima landslides triggered by rainstorm (Wang et al., 2015) and 2015 Shenzhen landslide (Ouyang et al., 2017; Yin et al., 2016). Many loess landslide in the original slope also showed fluidization progress, which were characterized by rapid movement and long runout distance (Peng et al., 2018; Qi et al., 2018; Xu et al., 2020; Zhang et al., 2017). Many rock avalanche deposits are composed of a large amount of non-plastic fines such as La Reunion Island debris avalanche deposits (Perinotto et al., 2015), rock avalanche deposits of Tschirgant in Austria and Flims in Swizerland (Dufresne et al., 2016; Dufresne and Dunning, 2017), these fine grains could be called by rock powder or rock flour, generated by inter-particles collision, fragmentation, disintegration, pulverization or gain crushing (Davies et al., 1999; Davies and McSaveney, 2009; McSaveney and Davies, 2007; McSaveney and Davies, 2006; Perinotto et al., 2015; Sassa et al., 1996; Siman-Tov and Brodsky, 2018), which involves the physical progress by which clasts and particles are reduced in size without chemical change, and some rock avalanche deposits show “inverse grading”, with mean particle sizes fining from the surface to the base (Dufresne et al., 2018; Siman-Tov and Brodsky, 2018). Non-plastic fine particles were also founded in tailings landslides, such as Merriespruit tailings, some materials obtained at different locations around the failure scar during its post-failure investigation have as much as 95% finer than 75 μm (Fourie et al., 2001), Ishihara (1993) pointed out that the sand containing such fines with a dry surface texture free minerals will show a great potential to liquefaction, thus, tailing have been shown to illustrate a low resistance to liquefaction.

Recently Earthquake induced landslide and its secondary hazards effect has drawn scientists’ attention (Fan et al., 2019; Hu et al., 2018a; Zhang and Zhang, 2017). Wenchuan earthquake induced intensive coseismic landslides and landslide dams, many dams are composed of unconsolidated fine debris resulting from the fragmentation of landslide materials during transportation without chemical weathering, such as Yangjia gully rock avalanche (Li et al., 2021; Liao et al., 2019; Wasowski et al., 2021), Laoyinyan landslide (Fan et al., 2017) and Daguangbao landslide (Cui et al., 2017; Huang et al., 2011). Fig. 1 shows the Yangjia gully rock avalanche deposits triggered by 2008 Wenchuan earthquake, large amount of fine particles and cracks generated by dynamic fragmentation were observed in the deposits, and local secondary failure phenomenon occurred on the deposits. Recent study revealed that the secondary landsliding phenomena and hazard chain effect had been widely triggered on these landslide deposits, and the initiation and movement of these landslides are greatly related to the involvement of no plastic fine materials resulting from mechanical fragmentation, because these fines

did not suffer from chemical weathering during the short period after earthquake.

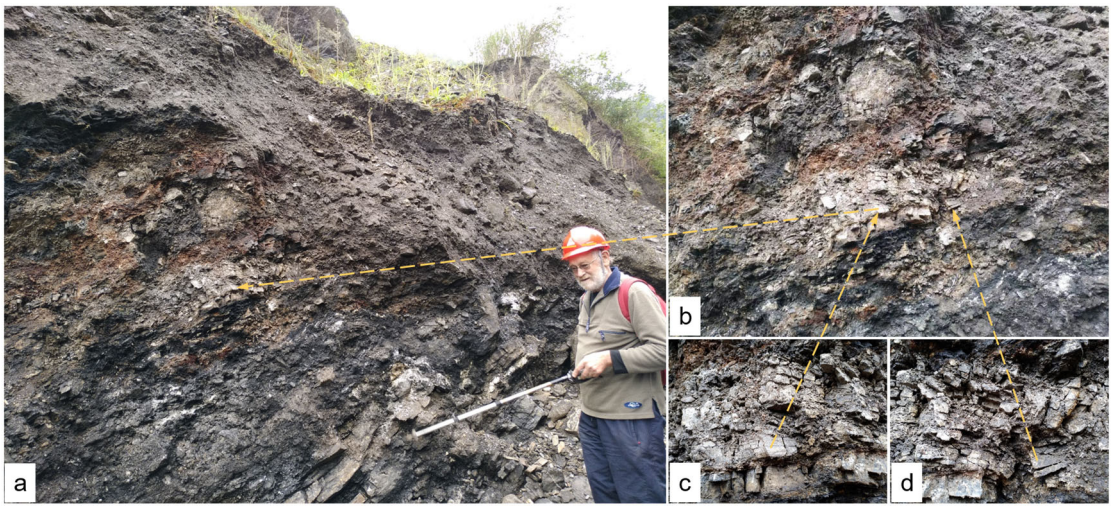

Fig. 1. Yangjia gully rock avalanche deposits triggered by 2008 Wenchuan earthquake. (a) Deposits of Yangjia gully rock avalanche, the deposits rich in non-plastic fines caused by dynamic fragmentation and grain crush, and local secondary failure phenomena occurred. (b) Enlarge part of figure 1a. (c) and (d) Enlarge part of figure 1b, many small fractures were observed. The picture was taken in the field investigation for International Research Association on Large Landslide (iRALL) School 2019 international doctorate program.

Here, It should be noted that the fine materials in this study were generated by physical weathering of original natural slope, grain crushing, mechanical fragmentation and dynamic disintegration (dynamic fragmentation) in landslide progress et.al physical process without chemical weathering involved, belong to the non-plastic fines, and rock powder/flour is a kind of this non-plastic fines. Many researcher focused on the plastic fines such as clay particles or loess effect (Chang and Wang, 2022; Chen et al., 2010; Gratchev et al., 2006; Jurko et al., 2008; Saito et al., 2007; Wang and Sassa, 2003, 2001), and some models including soil aggregates model (Iverson et al., 2010) and attraction-detachment model (Kluger et al., 2017) were proposed. However the non-plastic fines effect on the initiation and movement of landslides was not well understood. Several effect mechanisms of fine particles were posed: 1. effect of fine contents on behavior of liquefaction, and effect of non-plastic fines on the liquefaction resistance (opposite to the liquefaction potential) of sands appears to result in conflicting conclusions due to the differing results obtained from previous researches. According to the results of some studies, presence of non-plastic fines increase the liquefaction resistance of sands (Amini and Qi, 2000; Kwa and Airey, 2017; Ni et al., 2004; Pitman et al., 1994), while results of some other laboratory studies show a decrease of liquefaction resistance with increasing non-plastic fines content (Monkul et al., 2017; Monkul and Yamamuro, 2011; Murthy et al., 2007; Yamamuro and Lade, 1997), and some studies proposed a fines content (*FC*) threshold / limiting fines content (*LFC*) around which the proportion of non-plastic fines have a positive or negative effect (Bahadori et al., 2008; Chen et al., 2020; Dash and Sitharam, 2009; Papadopoulou and Tika, 2008; Polito and Martin II, 2001; Porcino and Diano, 2017; Rahman and Sitharam, 2020; Rahmani and Abolhasan Naeini, 2020; Thevanayagam et al., 2002; Yang and Wei, 2012; Zuo and Baudet, 2015). 2. Reducing the collision rate between coarser particles (Perinotto et al., 2015). 3. Fine-grained matrix itself and dust suspension model proposed (HSÜ, 1975). Among them, most understanding of non-plastic fines effect about liquefaction aspect has relied almost entirely on simple element testing of small specimens under idealized conditions, lack of landslide modeling experiments

verification. Cui et al. (2017) highlights fine particle migration in soil contributed to the soil failure and debris flow initiation by conducting flume experiments. Hu et al. (2018, 2017) carried out a series of flume tests with pore pressure and vibration signal transducers by identifying a threshold size d = 0.5 mm to discriminate between the small and the coarse materials, showing small particles in loose deposits played a role in triggering instability, failure and fluidization of the granular deposits, further demonstrated the major role of the internally erodible small grains in triggering, fluidization progress and producing grain coarsening. However, Furuya et al. (1999) pointed out that the fine materials can be eroded and transported by groundwater flows, resulting in enlarge voids and increasing susceptibility to failure of the landslide mass.

In this research, in order to get a deeper insight into the effect of non-plastic fines content on the initiation and movement of rainfall-induced landslides, a series of laboratory flume tests have been performed. Basic soil mechanical tests and Scanning Electron Microscopy (SEM) test have been carried out to investigate the basic properties and microstructure of samples. In addition, in the flume tests, cameras and image analysis method (Bryant et al., 2014; Ge et al., 2020; Krýza et al., 2019; Li et al., 2021; Qi et al., 2017; Sarno et al., 2018; Stanier et al., 2016; Stanier and White, 2013; Take et al., 2014, 2004; Taylor and Brodsky, 2020; Teng et al., 2020; Thielicke and Stamhuis, 2014; Wei et al., 2020; Zorn et al., 2020) have been used to visualize the initiation and movement of triggered landslides, pore water pressure (PWP) and tilting angle of soil mass variation have been monitoring by means of PWP sensors and tilting transducers. This study could provide valuable insights into failure behavior of fluidized landslide and then enhance understanding for catastrophic geohazards, which could provide the whole progress hazard chain information for landslides and landslide dams.

2. Methods

2.1 Materials

To study effects of fine particles content in the research, the samples used in the flume tests were sand-silt mixtures by adding silt in various percentages (by weight) to the clean host sand. In this work, silica sand no. 7 and silica powder # 100 were selected as the clean host sand and silt materials respectively. It is worth remarking that silica powder could be classified as rock flour, as their grains were formed by mechanical grinding with physical process. Silica sand no. 7 was comprised of subangular and angular quartz and feldspar, silica powder was composed of SiO_2, Al_2O_3 and Fe_2O_3 mineral materials. In the present study, a series of tests was conducted on the mixture of silica sand no. 7 and silica powder with silica powder content of 0%, 10%, 20%, 30% and 40% by weight. Fig. 2a shows the grain size distributions of silica sand no. 7 and silica powder respectively, Fig. 2b shows the microstructure of silica powder by scanning electron microscope (SEM), SEM imaging shows that silica powder consist of angular silica fines and shells with tens of microns in diameter and uniform shapes that tend to randomly distributed on the electrode surface, which confirms that fines used in study are produced by mechanical crushing. Fig. 3a illustrates the permeability of mixtures against void ratio. The maximum and minimum void ratios (e_{max} and e_{min}) of tested samples with various non-plastic fines content (FC) are presented in Fig. 3b. Properties of these samples are shown in Table 1.

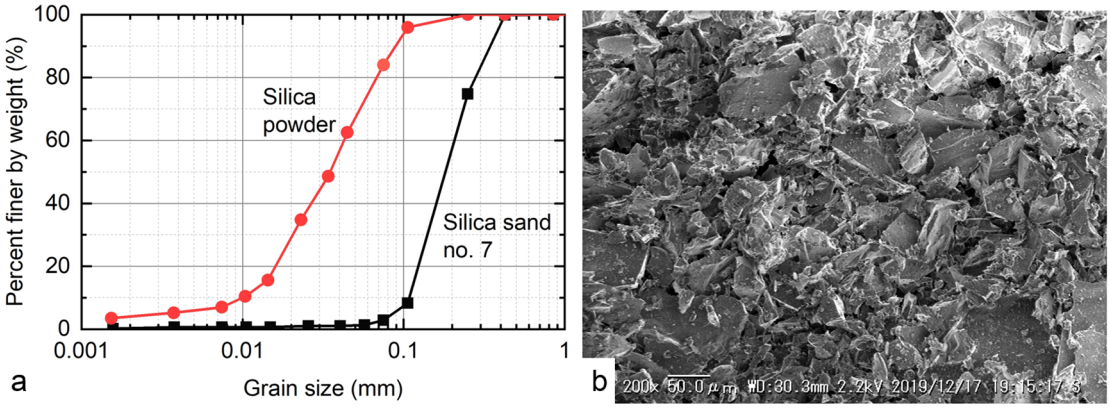

Fig. 2. (a) Grain size distributions of silica sand no. 7 and silica powder respectively. (b) Scanning electron microscope (SEM) imaging for fines, showing silica powder consist of angular silica fines and shells with tens of microns in diameter and uniform shapes that tend to randomly distributed on the electrode surface.

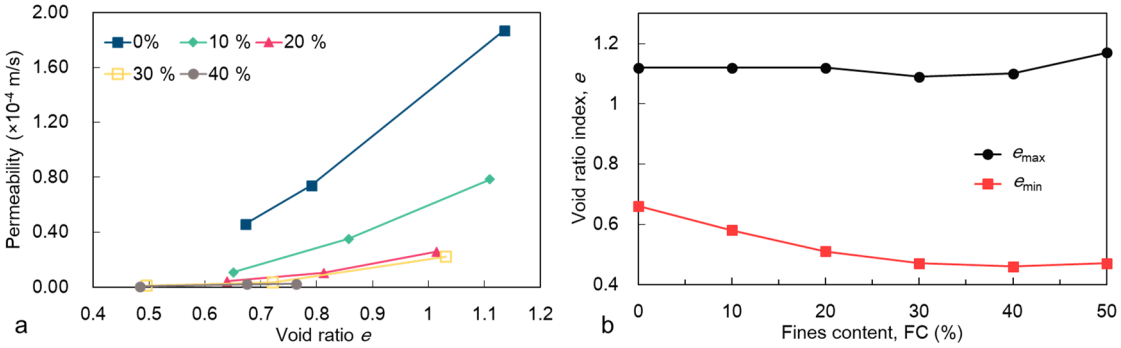

Fig. 3. (a) Permeability of mixture of silica sand no. 7 and silica powder with silica powder content of 0%, 10%, 20%, 30%, 40% by weight. (b) Maximum and minimum void ratios (e_{max} and e_{min}) of tested samples with various non-plastic fines content (FC).

Table 1. Properties of employed samples.

Sample	Particle density	Minimum dry density	Maximum dry density
	ρ_s (g/cm^3)	ρ_{dmin} (g/cm^3)	ρ_{dmax} (g/cm^3)
S7-0	2.63	1.24	1.58
S7-10	2.63	1.24	1.66
S7-20	2.63	1.24	1.74
S7-30	2.63	1.26	1.79
S7-40	2.63	1.25	1.80

Note: The sample employed in the study is mixture of silica sand no. 7 and silica powder with silica powder content of 0%, 10%, 20%, 30% and 40% by weight, which were termed S7-0, S7-10, S7-20, S7-30 and S7-40 respectively.

2.2 Experimental setup and test procedure

2.2.1 Flume test apparatus setup

The tests have been conducted by experimental flume. The employed experimental apparatus were showed in Fig. 4a. The flume was 200 cm in length, 25 cm in width and 40 cm in height, with a floor inclination of 25° from the horizontal. The side wall of experimental fume consisted of transparent plexiglass sheets, and the surface of flume base was covered by rubber sheet glued by sand grains to reproduce suitable frictional contact and prevent base sliding. As shown in Fig 4a, the landslide model was designed as a trapezoid, the size of slope model was illustrated in Fig. 4b. In the model, 7 measuring point locations (P1~P7) were selected to install the sensors (Fig. 4b). As shown in Fig. 4b, 6 pore water pressure (PWP) transducers were installed within the soil mass at different depths (5 and 10 cm vertical distance to base of flume) to measure the pore water pressure, and additional 4 pore pressure sensors were installed at the bottom of the flume. 7 tilting sensors were used to catch the variations of rotation-angle inside soil mass due to the movement of soil, among them, 3 tilting sensors were installed to close to the PWP sensors (P1~P3 location with 10 cm vertical distance to base of flume), 4 tilting sensors were installed closely to the base of flume and PWP sensors at bottom (P4~P7 location bottom). At the bottom of P6 location, a styrene foam ball in 2 cm diameter was used to capture the sliding displacement of soil mass in the sliding process. This foam ball was connected with a linear displacement sensor placed at the back and upslope of flume through a stiff wire. A laser displacement sensor was used to get more precise movement of foam ball by shining a laser beam to the fixed target connecting with the ball. A 150 g counterweight was utilized to balance the pulling resistance of installed linear displacement sensor. Artificial rainfall (100 mm/h) from two sprinklers mounted above the flume was used to trigger landslides (Fig 4a). Two video cameras respectively located at front and side wall were used to obtain the entire dynamic process of triggering landslides, and technical image analysis was performed to evaluate the deformation and movement of the slope.

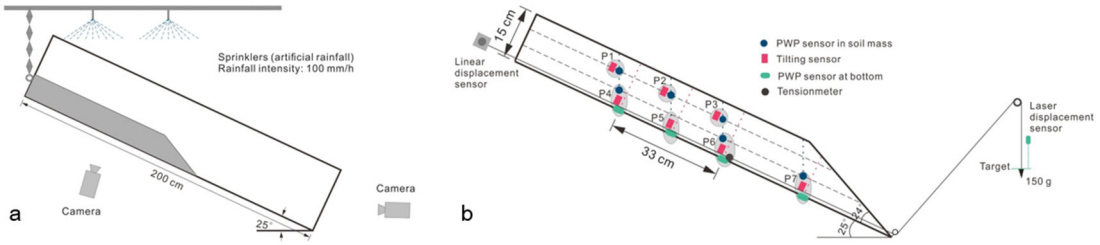

Fig. 4. (a) Employed experimental flume (200 cm in length, 25 cm in width and 40 cm in height). (b) Arrangement of experimental apparatus and set-up of various sensors. 7 measuring point locations (P1~P7) were selected. At location of P1, P2, P3, both 3 pore water pressure (PWP) sensors and 3 tilting sensors were used. At location of P4, P5, P6 and P7, 3 PWP sensors were installed in the inner soil mass at the location with 5 cm vertical distance to bottom of flume (middle of P4, P6 and P7 location), 4 PWP sensors were installed at the bottom of flume (bottom of P4, P5, P6 and P7 locations), 4 tilting sensors were installed closely to the base of flume and PWP sensors at bottom (P4~P7 locations bottom). At P6 location, a foam ball was used to monitor the displacement of soil mass by linear displacement transducer and laser displacement sensor respectively.

2.2.2 Flume test procedures and conditions

The flume tests have been carried out using mixtures of silica no. 7 and silica powder containing 0%, 10%, 20%, 30% and 40% of fines in dry weight, and soil mixtures was prepared at an initial gravimetric water content of 10%. Pore water pressure (PWP) transducers and displacement sensor at bottom of flume were installed first, after installation of these sensors, the prepared mixtures were placed in the

flume and gently compacted later in the successive layers. To make the samples uniform as much as possible, the sample was placed in 6 layers, each layer was parallel to the base of flume and later tamped gently to the successive thickness of about 2 to 3 cm, the weight of each layer samples was set as 1/6 total weight. To ensure tilt sensor at flume bottom could rotate freely and measure the same location of PWP sensors as soon as possible, after placing and tamping the first soil layer, 4 tilting sensors was carefully installed close to the base of flume and PWP sensors at bottom of P4, P5, P6 and P7 location. After placing and tamping all 6 soil layers, the sample was shaped subsequent by removing the superfluous parts of the sample as shown in Fig. 4a. The data recording system from all sensors and video camera were activated with a sampling frequency of 20 Hz when water began to sprinkle. The landslide velocities were calculated through comprehensive analysis based on the displacement data measured by linear displacement transducer and image analysis technique. If the failed landslide mass movement is slow, the velocity was calculated by displacement monitored by liner displacement sensor, if movement is fast or sliding depth is shallow, the velocity was calculated through displacement captured by image analysis (Thielicke and Stamhuis, 2014).

To study different densities effects of mixtures, we conducted the experiments by mixture containing same fines content with various dry densities. Table 2 illustrates test conditions and summarized data in all flume tests. In flume tests, the flume angle was kept at 25°, artificial rainfall intensity was kept as 100 mm/h. The experimental flume tests were carried out in 5 series including 25 tests: series 1, tests on S7-0; series 2, tests on S7-1; series 3, tests on S7-2; series 4, tests on S7-3; series 5, tests on S7-4. Each series was conducted by 5 tests using same samples with different dry densities, correspondingly, relative density D_r ($D_r = (\rho_d - \rho_{min}) / (\rho_{max} - \rho_{min})$) of each sample used in the experimental test was calculated and compared.

3. Results

3.1 Observed major Landsliding phenomena and failure modes

The landslide failure phenomena are quite different in the flume tests, which greatly depends on the sample's density and fine particles content of employed mixtures. According to recordings of videos, the observed general phenomena in the soil mass sliding process could be simply categorized as following stages: wetting, precursory slides, then major failure followed, as suggested by Wang and Sassa (2003). The soil mass became wet after sprinkling, the wetting front gradually closed to the flume base with approximately parallel to the floor of flume, after a while when wetting front reached the flume base, small precursory slides occurred, then followed by major failure. The landslide behaviors are quite different during major failure period. Fig. 5 shows the summarized landslide type and failure mode in major failure period of landslides according to the landslide phenomenon. The summarized failure modes were divided into 5 types (Fig. 5). Type 1 is slow individual sliding, which was characterized by entire inconsistent retrogressive sliding behavior, the soil mass in some tests slipped episodically, displaying repeated slip episodes. In the retrogressive sliding process, the next single soil block moved after former soil block slumping and sliding downward, and the individual sliding soil block moved slowly with small volume. As shown in Fig. 5, the duration for individual soil block sliding in type 1 is about tens of seconds. Type 2 is sudden multiple sliding, showing several soil blocks were formed at almost same time in the short periods (almost 1 s) with multiple features, then formed multiple soil block moved slowly in the lateral progress. Type 3 is fast individual sliding, which was also characterized by entire retrogressive sliding behavior with similarity of phenomenon in type 1, what featured difference is the individual sliding soil block moved fast in flowslide motion with small volume (Fig. 5). Type 4 is fast deep overall

sliding, which was characterized by entire rapid flowslide motion. The fluidized landslide block moved fast with large volume and deep sliding surface, comparing to type 3, the sliding mass volume is much larger than that in type 3. Type 5 is fast shallow overall sliding, which was characterized by entire rapid flowsliding, the soil mass moved rapidly and had shallow sliding surface, which was different from type 4.

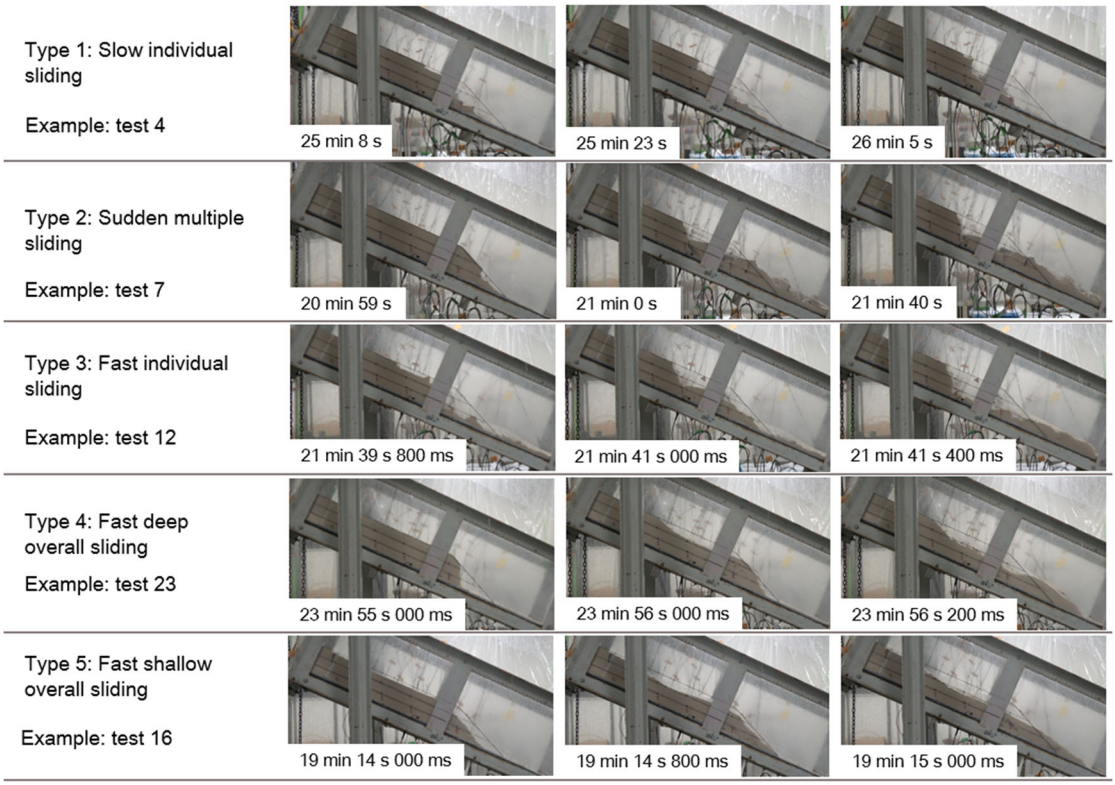

Fig. 5. Summarized landslide type and failure mode in major failure period of landslides. The observed major Landsliding phenomena are divided into 5 types, and the initial time was set as the beginning of rainfall.

3.2 Tilting of soil mass in slide episode and pore water pressure variation with soil rotation

3.2.1 Tilting of soil mass in slide episodes

Various landslide phenomena could be surprisingly captured by tilting of soil, corresponding to the various landslide failure modes, the tilting of soil mass showed quite different performance with the soil mass movement. Fig. 6a presents the typical tilting variation in the landslide type 1 with slow individual sliding of test 4, revealing retrogressive sliding characters on the whole. The soil mass at P7 location began to gradually rotate first at 1420 s, then followed by soil at P3 and P6 location that slowly rotated at 1603 s and 1566 s (Fig. 6a, b and c). Then soil at P2 and P5 location started rotation at 1727 s and 1769 s (Fig. 6a, d). Last, soil mass located at P1 and P4 location began to tilt at 2094 s and 2097 s with slow velocity. The results of tilt indicated the landslide in this test could be characterized by retrogressive sliding and each single sliding block moved slowly.

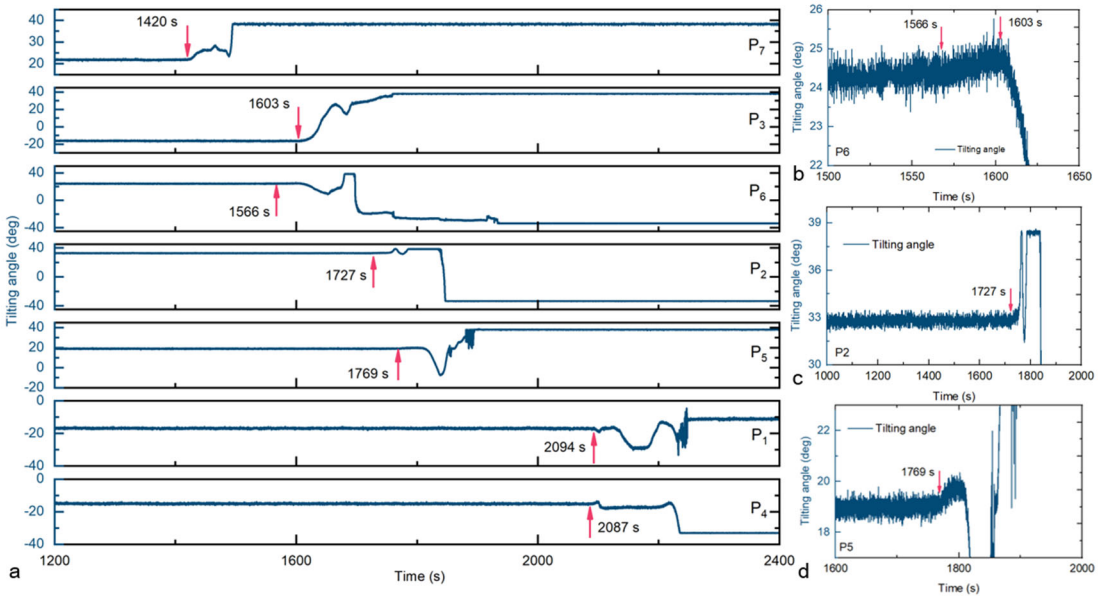

Fig. 6. (a) Typical tilting variation in the landslide type 1 with slow individual sliding of test 4, and retrogressive sliding observed by tilting variation. (b) Enlarge part of Fig. 6a at P6 location. (c) Enlarge part of Fig. 6a at P2 location. (d) Enlarge part of Fig. 6a at P5 location.

Fig. 7a shows the tilting results of test 7 with sudden multiple sliding in type 2. As shown, the soil mass at location of P7, P3, P6, P2, P5 suddenly rotated at almost same time (1379.2 s and 1378.9 s) and stopped soon, showing a rapid and straight changing tilting curve, which is quite different from those in type 1. Then soil mass began to restart to rotate due to the continuing rainfall at about 1421 s, and followed by the rotation of soil mass at location of P1 and P4. In this test, the tilting variation of soil showed a typical multiple sliding. Fig. 7b presents the results of test 12 with fast individual sliding in type 3. The soil mass at P7 location began to rotate first at 1290.1 s, then followed by soil at P3 and P6 location that rotated at 1309.1 s and 1309.2s. The soil at P2 and P5 location started rotation at 1322.5 s and 1322.6 s after rotation of previous soil block. Last, soil mass located at P1 and P4 location began to tilt at 1474.4 s. These results of tilting in the test 12 suggested the landslide mode was characterized by retrogressive landsliding in the whole. Although similar retrogressive landslides occurred in type 3 and type 1, a big difference could be observed in type 3 as shown in Fig. 7b, each single tilting curve sharply increased or decreased with time, indicating the individual soil mass moved quickly, which is different from the slow motion of soil in type 1.

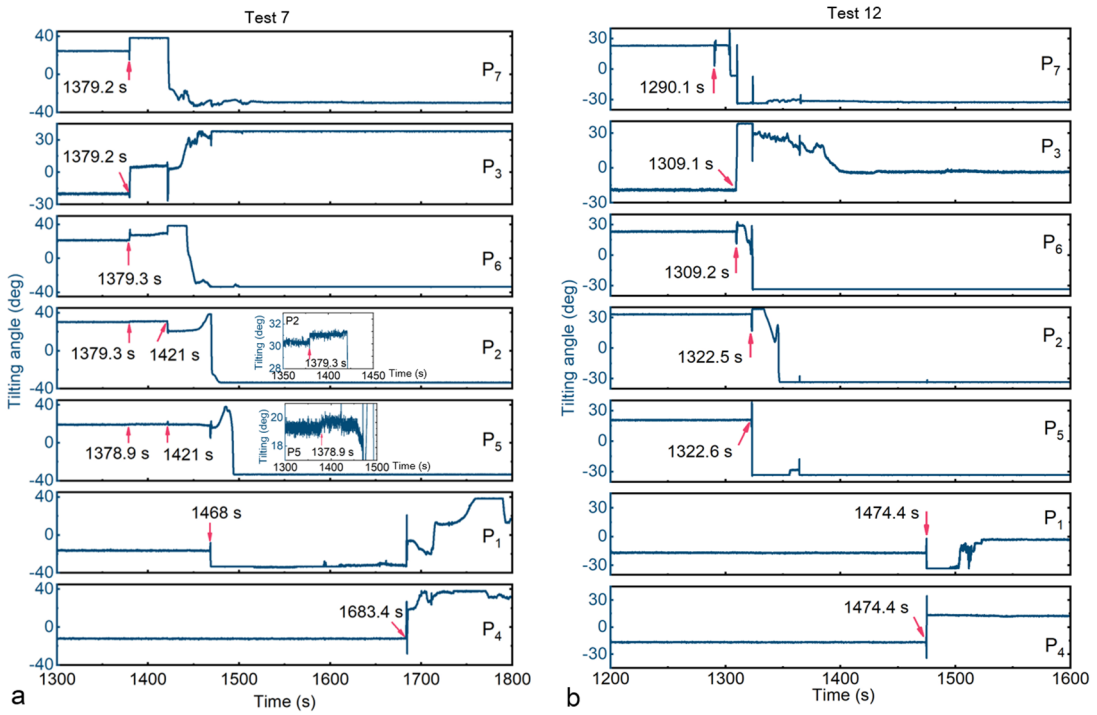

Fig. 7. (a) Typical tilting variation in the landslide type 2 with sudden multiple sliding of test 7. (b) Tilting variation in the landslide type 3 with fast individual sliding of test 12.

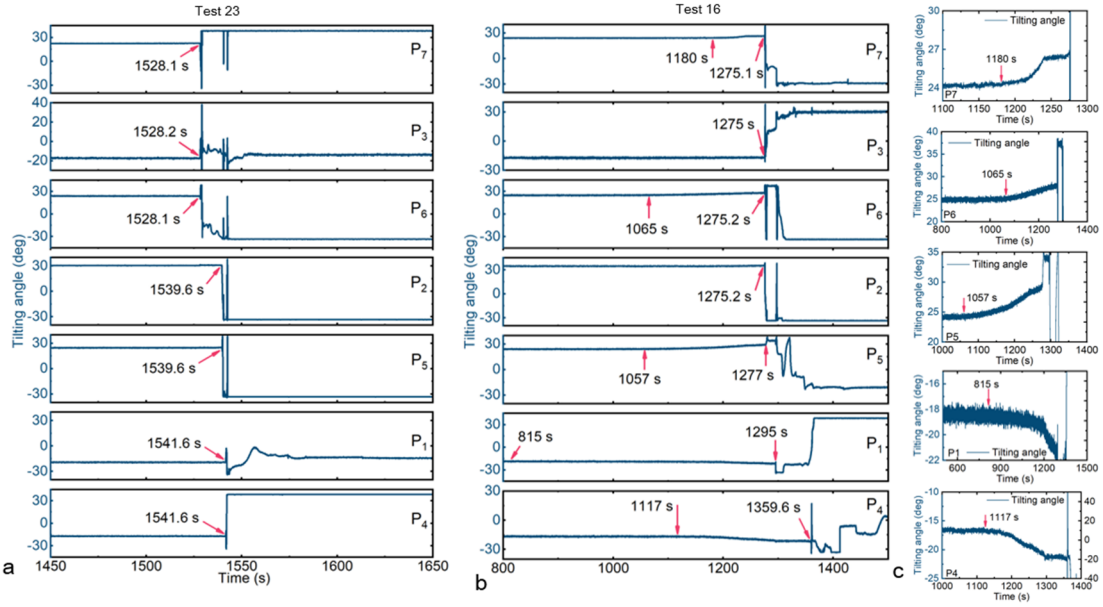

Fig. 8. (a) Typical tilting variation in the landslide type 4 with fast deep overall sliding of test 23. (b) Tilting variation in the landslide type 5 with fast shallow sliding of test 16. (c) Enlarge part of Fig. 8b at P7, P6, P5, P1 and P4 location respectively.

Fig. 8a shows the tilting results of test 23 with fast deep overall sliding in type 4. As shown, the soil mass at location of P7, P3 and P6 suddenly rotated together at almost same time (1528.1 s and 1528.2 s) a, showing a sharp and straight changing tilting curve. Then soil mass at P2 and P5 location began to rotate at about 1539.6 s, and followed by the rotation of soil mass at location of P1 and P4 (1541.6). In this test, the tilting variation of soil showed the soil mass at P7, P3 and P6 failed and quickly moved at

the same time, indicating the volume of single soil block is higher than that in type 3, which illustrate an overall failure and movement. Fig. 8b presents the results of test 16 with fast shallow overall sliding in type 5. The soil mass at P7, P3, P6, and P2 location began to rapidly rotate together at about 1275 s, then followed by soil at P5 location that rotated at 1277s (later than 1275 s), this result suggested the soil mass moved fast with big size and shallow sliding surface. Last, soil mass located at P1 and P4 location began to heavily tilt at 1295 s and 1359.6 s. Before the movement of failed soil mass, the settlement was evidenced by a slight rotation of subsurface tiltmeters (Fig. 8c), which is similar to the results proposed by Iverson (2000). As shown in Fig. 8c, the slight rotation of tiltmeters at different locations has different initiation time and lasted for a certain time before the movement of soil mass.

3.2.2 Pore water pressure variation and sliding displacement corresponding to the soil rotation

To study the pore water pressure (PWP) variation and sliding displacement with the soil rotation progress, we focused on the results of transducers located at P6 (Fig. 4b). Fig. 9a shows the overall tendency of results of transducers at location P6 (test 25) during the slow individual sliding in type 1. As shown, PWP at bottom gradually increased at about 1372s, and reached a plateau then a small local built up observed, lastly PWP sharply decreased. The PWP in the soil gradually increased first and then declined. The tilting angle curve showed a slow growth first after 1500 s and then fluctuated with soil rotation. The landslide displacement measured by laser sensor and linear transducer presented an increasing tendency when soil began to rotate. To illustrate the detail information, the enlarge part of Fig. 9a from 1495 s to 1560 s was showed in Fig. 9b. As shown, the local built up of PWP at bottom could be observed with the soil rotation first, suggesting excess pore water pressure generated during soil deformation and failure. Then PWP at bottom decreased after reaching peak value with time, however, the PWP in the inner soil mass had reached the peak value before the rotation of soil, when soil began to rotate, the PWP in the inner soil mass began to decline from the peak. Tilting angel gradually increased first at about 1527 s and then sharply decrease at about 1543 s. the slight sliding displacement measured by laser sensor slowly increased in the progress of soil gradual rotation, which could not be caught by linear transducer, however, when the tilting angle dramatically decreased, the macro sliding distance measured by linear transducer was observed to increase, these results indicate tilting variation is more sensitive than sliding, and is prior to the sliding of soil mass in this test.

Fig. 10a shows the overall tendency of results of transducers at location P6 (test 7) during the sudden multiple sliding in type 2. As shown, the soil suddenly rotated at about 1380 s and stopped soon, later restarted at around 1421 s, which is consistent with the macro sliding displacement arrested by linear transducer, displaying repeated slip episodes. The PWP at bottom gradually increased first and soared before the first rotation of soil mass, and then decreased with tilting of soil mass. Fig. 10b showed the enlarge part of Fig. 10a from 1360 s to 1390 s, as shown, when the soil began to rotate, the PWP at bottom decreased from the peak value, the PWP in the soil mass had a fluctuation, at the same time, the sliding distance captured by linear sensor began to increased, before the observed macro displacement of linear displacement sensor, a slight increasing of sliding displacement arrested by laser sensor.

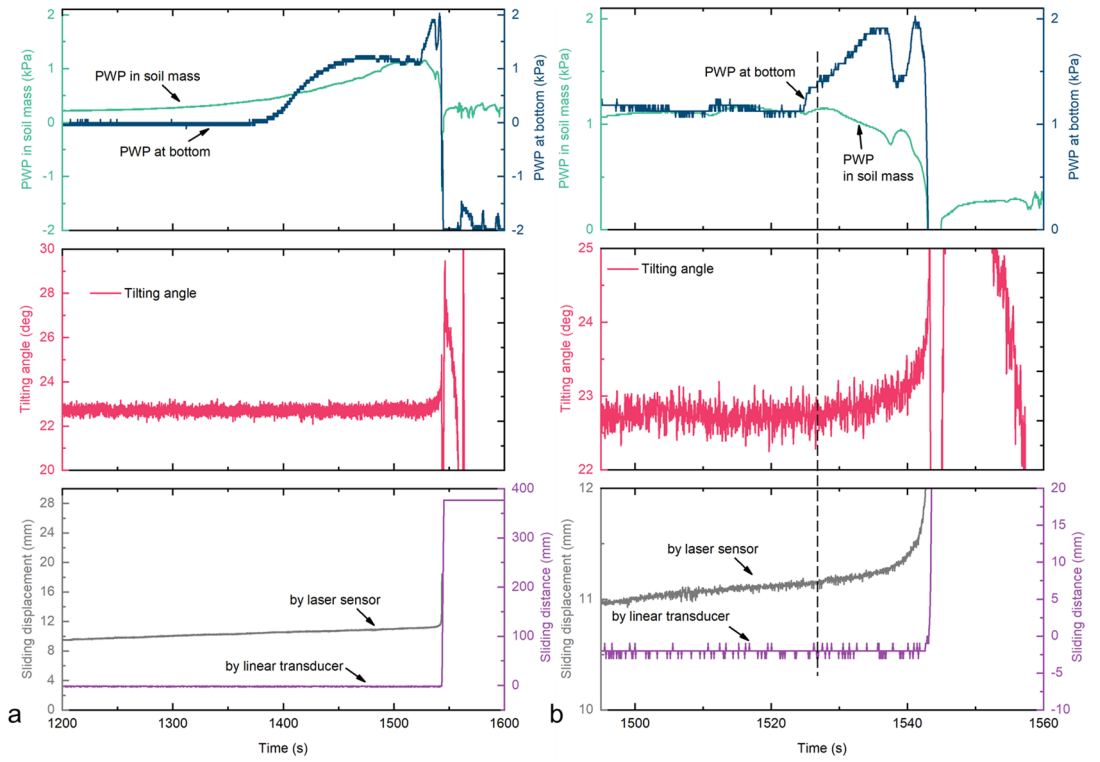

Fig. 9. (a) Results of transducers at location P6 (test 25) during the slow individual sliding in type 1. (b) Enlarge part of Fig. 9a from 1495 s to 1560 s.

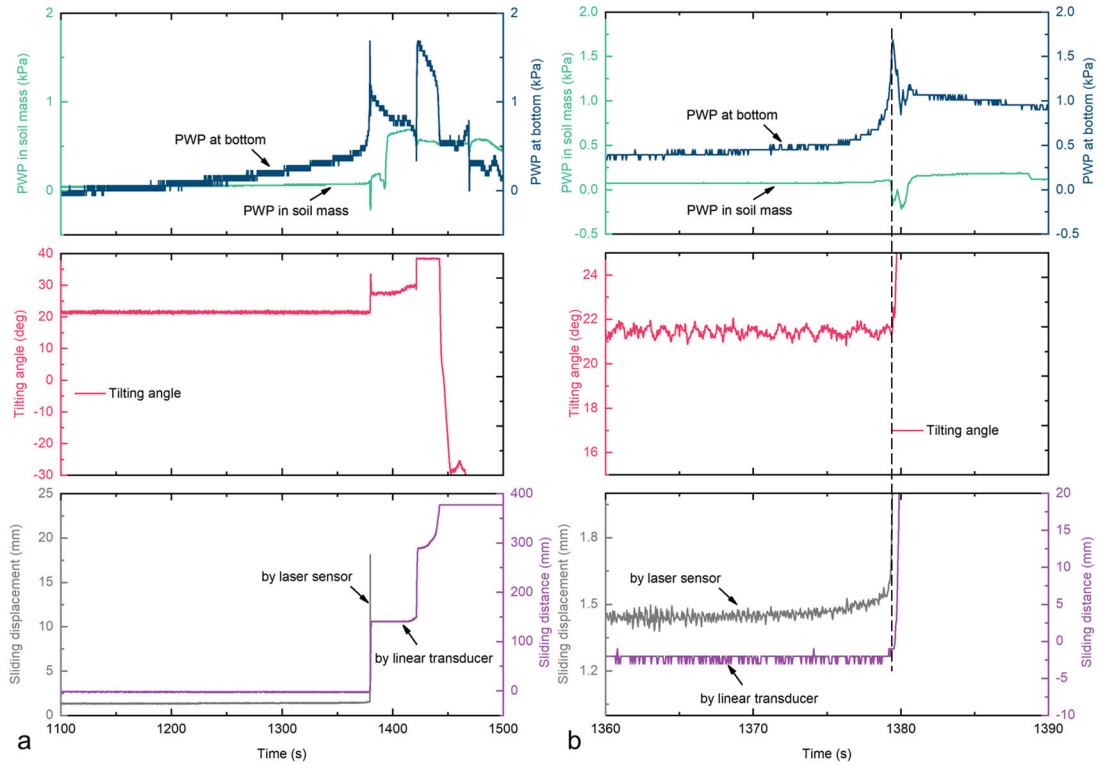

Fig. 10. (a) Results of transducers at location P6 (test 7) with sudden multiple sliding in type 2. (b) Enlarge part of Fig. 10a from 1360 s to 1390 s.

Fig. 11a shows the overall tendency of results of transducers at location P6 (test 12) with fast individual sliding in type 3. As shown, the soil suddenly rotated at about 1309 s and sliding displacement sharply increased at same time. The PWP at bottom gradually increased first and soared before the rotation of soil mass, and then decreased with tilting of soil mass. Fig. 11b showed the enlarge part of Fig. 11a from 1300 s to 1320 s, as shown, when the soil began to rotate, the PWP at bottom decreased from the peak value, on the contrast, the PWP in the soil mass had a small built up after soil rotation. In this test, the sliding displacement arrested by both laser sensor and linear transducer began to increase with sharp curve when the soil began to rotate.

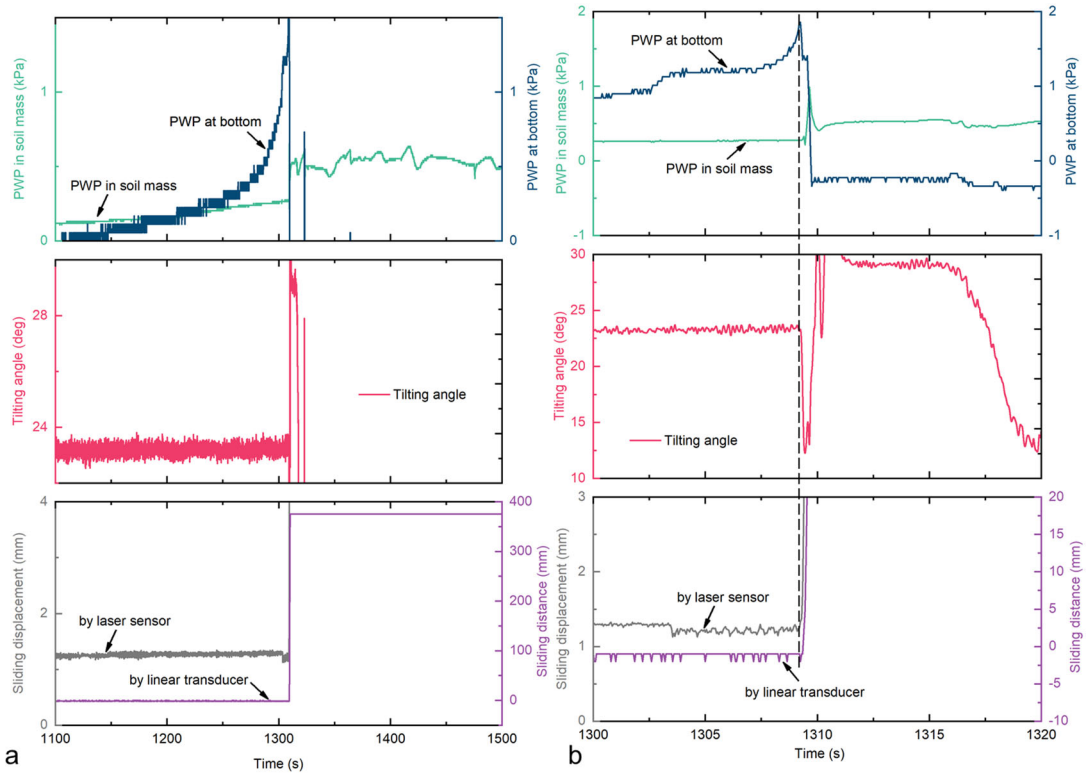

Fig. 11. (a) Results of transducers at location P6 (test 12) with fast individual sliding in type 3. (b) Enlarge part of Fig. 11a from 1300 s to 1320 s.

Fig. 12a shows the overall tendency of results of transducers at location P6 (test 17) with fast deep overall sliding in type 4. As shown, the soil showed a sudden rotation and sliding displacement sharply increased at same time. The PWP at bottom gradually increased first and then gradually decreased before the rotation of soil mass, then fluctuated with tilting of soil mass. Fig. 12b showed the enlarge part of Fig. 12a from 1400 s to 1410 s, as shown, when the soil began to rotate, the PWP both at bottom and in soil increased first and decreased soon, and the small built up of PWP occurred after soil rotation. In this test, the sliding displacement arrested by both laser sensor and linear transducer began to increase with sharp curve when the soil just began to rotate.

Fig. 12c shows the overall tendency of results of transducers at location P6 (test 23) with fast deep overall sliding in type 4. As shown, the soil showed a sudden rotation and sliding displacement sharply increased in this test. The PWP at bottom gradually increased first and then sharply decreased with the rotation of soil mass, PWP in soil show fluctuation with tilting of soil mass. Fig. 12d showed the enlarge part of Fig. 12c from 1525 s to 1530 s, as shown, when the soil began to rotate, the PWP at bottom decreased from the peak value, on the contrast, the PWP in the soil mass had a small built up after soil

rotation. In this test, the tilting of soil is prior to the sliding displacement increasing with sharp curve arrested by both laser sensor and linear transducer.

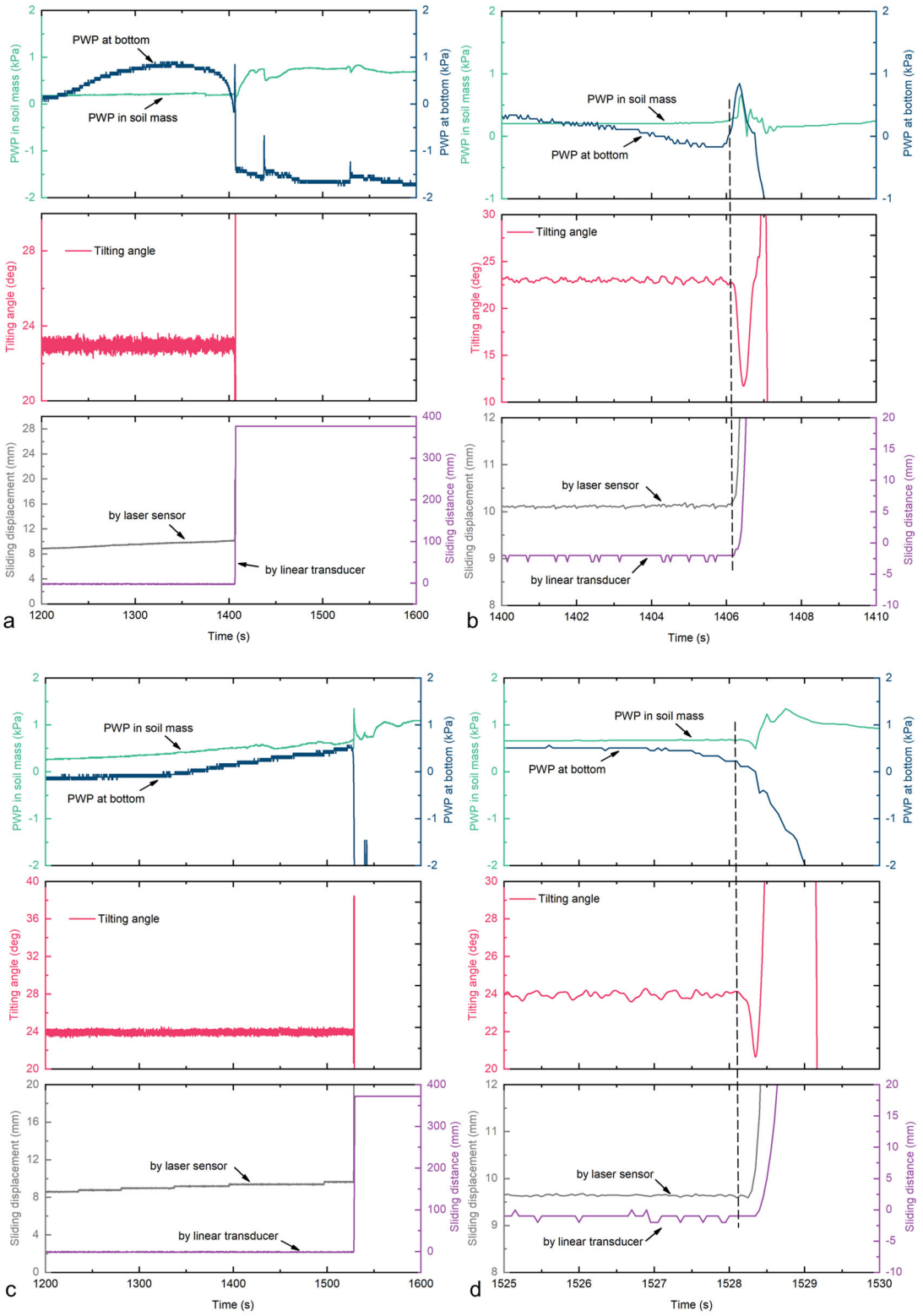

Fig. 12. (a) Results of transducers at location P6 of test 17 with fast deep overall sliding in type 4. (b) Enlarge part of Fig. 12a from 1400 s to 1410 s. (c) Results of transducers at location P6 of test 23 with fast deep overall sliding in type 4. (b) Enlarge part of Fig. 12c from 1525 s to 1530 s.

Fig. 13a shows the overall tendency of results of transducers at location P6 (test 16) with fast shallow overall sliding in type 5. As shown, the soil showed a gradual rotation first and then a rapid fluctuation occurred. The sliding displacement measured by laser sensor gradually increased first and then rapid grew. The PWP at bottom gradually increased first and then gradually decreased before the rotation of soil mass, then fluctuated with tilting of soil mass. Fig. 13b showed the enlarge part of Fig. 13a from 1270 s to 1280 s, as shown, when the soil began to rotate, the PWP both at bottom and in soil increased first and decreased soon, and the small built up of PWP occurred after soil rotation. In this test, the tilting of soil is prior to the sliding displacement increasing arrested by both laser sensor and linear transducer.

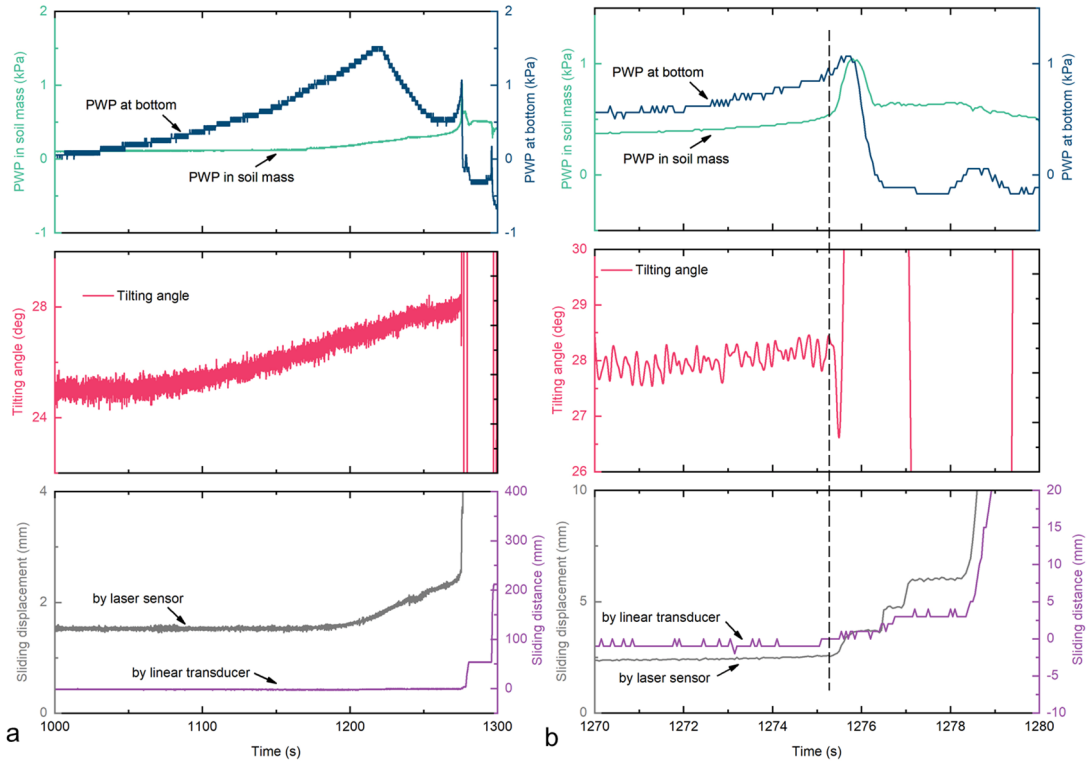

Fig. 13. (a) Results of transducers at location P6 of test 16 with fast shallow overall sliding in type 5. (b) Enlarge part of Fig. 13a from 1270 s to 1280 s.

3.3 Displacement and velocity of landslides

The variation of sliding velocity and sliding distance for employed samples is showed in Fig. 14. As shown in Fig. 14a, for the test 4 on S7-0 in type 1, the sliding mass accelerated until reached a first velocity maximum, and then decreased and further fluctuated with sliding distance. Fig. 14b shows the results for test 25 on S7-4 in type 1, the sliding mass accelerated until reached a certain velocity, and then decreased and further fluctuated with sliding distance. Fig. 14c shows the results for test 7 on S7-1 in type 2, the sliding mass accelerated until reached a certain velocity, and decreased to a low point, and then accelerated again, last decreased to the certain low value with almost constant velocity. Fig. 14d, Fig. 14e, Fig. 14f and Fig. 14g show the results for test 12 on S7-2 in type 3, test 17 on S7-3 in type 4, test 23 on S7-4 in type 4 and test 16 on S7-3 in type 5 respectively, unlike the phenomena observed in Fig. 14a, b and c, the landslide mass moved continually without deceleration within the visible range in the flume test, which accelerated continuously, and the value of acceleration show a general decreasing tendency.

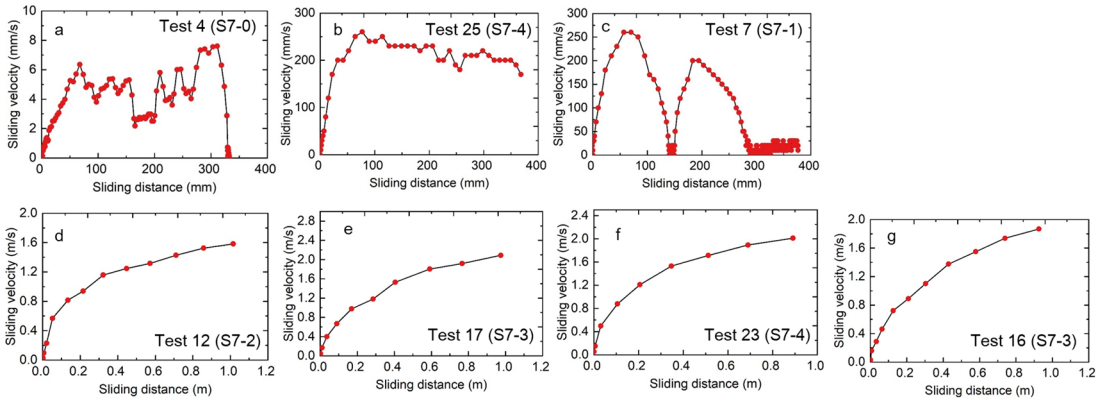

Fig. 14. Sliding velocity against sliding distance. (a) for test 4 on S7-0 with type 1. (b) for test 25 on S7-4 with type 1. (c) for test 7 on S7-1 with type 2. (d) for test 12 on S7-2 with type 3. (e) for test 17 on S7-3 with type 4. (f) for test 23 on S7-4 with type 4. (g) for test 16 on S7-3 with type 5.

4. Discussion

4.1 Fines content and relative density effects on landslide type and failure mode

The experimental flume tests performed on mixtures prepared with different non-plastic fines content and relative densities highlighted significant differences in the landslide type and failure modes. To clarify fines content and relative density effects on landslide type and failure mode, according to the phenomena observed, tilting angle variation and calculated landslide velocities of all 25 tests, we summarized fines content and relative density effects on the landslide type and failure mode (Fig. 15). As shown in figure 15a, the fines content and relative density play a critical role in the failure mode and landslide type, the landslide type illustrated a clear gradient variation trend with fines content increasing and relative density increasing. For the fines content effect, at almost same relative density of -0.54 ~ -0.52, landslide type transformed from sudden multiple sliding in type 2 (light pink area) to fast deep overall sliding in type 4 (green area) with fines content increased, however, when fines content reached and beyond 30%, the landslide type transformed from fast deep overall sliding to shallow overall sliding in type 5 (blue area). At relative density of -0.19 ~ -0.21, the failure mode transferred from slow individual sliding in type 1 (gray area) to fast individual sliding in type 3 (deep pink area) with fines content increased to 20%, and then changed from fast individual sliding in type 3 (deep pink area) to fast shallow overall sliding in type 5 (blue area) across fast deep overall sliding in type 4 (green area) successively with further increased fines content. At relative density of -0.04 ~ -0.06, the failure mode transferred from slow individual sliding in type 1 (gray area) to fast individual sliding in type 3 (deep pink area) with fines content increased to 30%, and then changed from fast individual sliding in type 3 to fast deep overall sliding in type 4 when fines content was as 40%, sudden multiple sliding in type 2 and fast shallow overall sliding in type 5 did not occur anymore. At relative density of 0.07 ~ 0.09, when the fines content was lower than 30%, the landslide mode were characterized by slow individual sliding in type 1, and it transformed to fast individual sliding in type 3 when fines content was at 40%. At relative density of 0.24 ~ 0.25, the landslide mode was constant characterized by slow individual sliding in type 1 with fines content increasing. For the relative density effect, the landslide failure mode changed from sudden multiple sliding in type 2 to slow individual sliding in type 1 with relative density increasing under no fines condition. The landslide failure mode changed from fast deep overall sliding in type 4 to slow individual sliding in type 1 with relative density increasing when fines content is 10%. The landslide failure mode changed from fast deep overall sliding in type 4 to slow individual sliding in type 1 crossing

fast individual sliding in type 3 with relative density increasing when fines content is 20%. Figure 15b shows the landslide types variation with increased relative density when the fines content is high (30% and 40%). The landslide mode changed from fast shallow overall sliding in type 5 to slow individual sliding in type 1 crossing fast deep overall sliding in type 4 and fast individual sliding in type 3 with relative density increasing, indicating relative density also plays an essential role in failure mode of landslides, slow individual sliding could occur when relative density is high although sample has high fine contents.

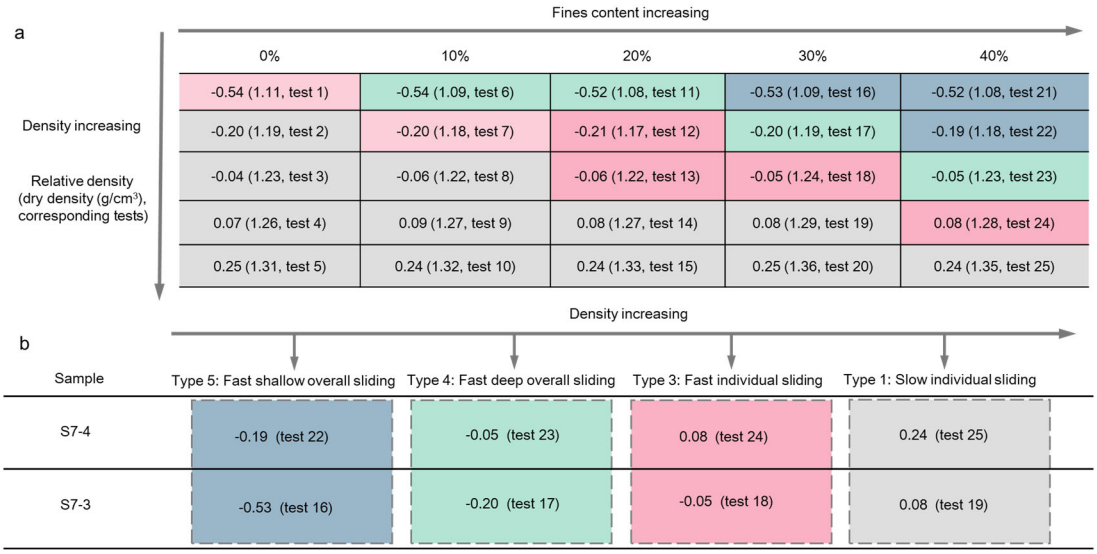

Fig. 15. (a) Fines content and relative density effects on summarized landslide type and failure mode. Gray area shows slow individual sliding in type 1, light pink area shows sudden multiple sliding in type 2, deep pink area shows fast individual sliding in type 3, green area shows fast deep overall sliding in type 4, blue area shows fast shallow overall sliding in type 5. (b) Detailed explanation examples on samples with S7-4 and S7-3 effected by increased relative density at high fines content condition.

4.2 Fines content and relative density effects on velocities of landslides

Fines content and relative density have great effects on the movements of landslides. To evaluate the movement characters of landslides, the maximum velocity was used in the progress of landslide. Figure 16a shows the maximum velocity variation against fines content, as shown, at relative density of -0.54 ~ - 0.52, the maximum velocity increased in general with fines content increasing to 30%, and then dramatically decreased when fines content was at 40%. An optimal fines content was also observed contributing to the maximum velocity at relative density of -0.21 ~ -0.19, this optimal fines content is 30%, which is consistent with results of mixtures with relative density of -0.54 ~ - 0.52. When fines content below 30%, a positive relationship was observed, while beyond 30%, the maximum velocity slightly deceased, although maximum velocity was still high. However, at relative density of -0.06 ~ -0.04, the maximum velocity increased in total with increased fines content, the biggest increasing was at 30% fines content. The relationship of maximum velocity and fines content at relative density of 0.07 ~ 0.09 and 0.24 ~ 0.25 was showed in Figure 16b, as shown, the maximum velocity showed a gradual growth tendency with increased fines content both at relative density of 0.07 ~ 0.09 and 0.24 ~ 0.25, and the maximum value of maximum velocity is quite smaller. These results suggested landslide rate has acute sensitivity to initial fines content around certain range. Figure 16c shows the maximum velocity variation against relative density, figure 16d shows detailed low velocity information of relative density effects on maximum velocity of landslides with fines content, which is enlarge part of Fig. 16c. As shown,

when fines content is low at 0% and 10 %, the maximum velocity decreased with relative density increasing. When the fines content is at 20%, the maximum velocity increased gradually with relative density increasing from -0.6 to around -0.2, but then decreased significantly with further increasing relative density, the threshold relative density was -0.2. Similar tendency (increasing first and decreasing later, threshold relative density was -0.2) occurred on the mixtures with 30% fines content, and the maximum velocity at relative density of -0.6 ~ -0.04 is much higher than that at relative density beyond -0.04, indicating landslide rate has acute sensitivity to initial relative density around this range. When the fines content is at 40%, the maximum velocity gradually increased with relative density increasing, but when relative density beyond -0.04, reverse tendency occurred, showing significant drop with further relative density, a threshold for relative density was found to be -0.04. From Fig. 16c and Fig. 16d, at high fines content (20%, 30% and 40%), the optimal relative density was observed to contributing to the maximum velocity of landslides, and the optimal relative density was at around -0.2 ~ -0.04.

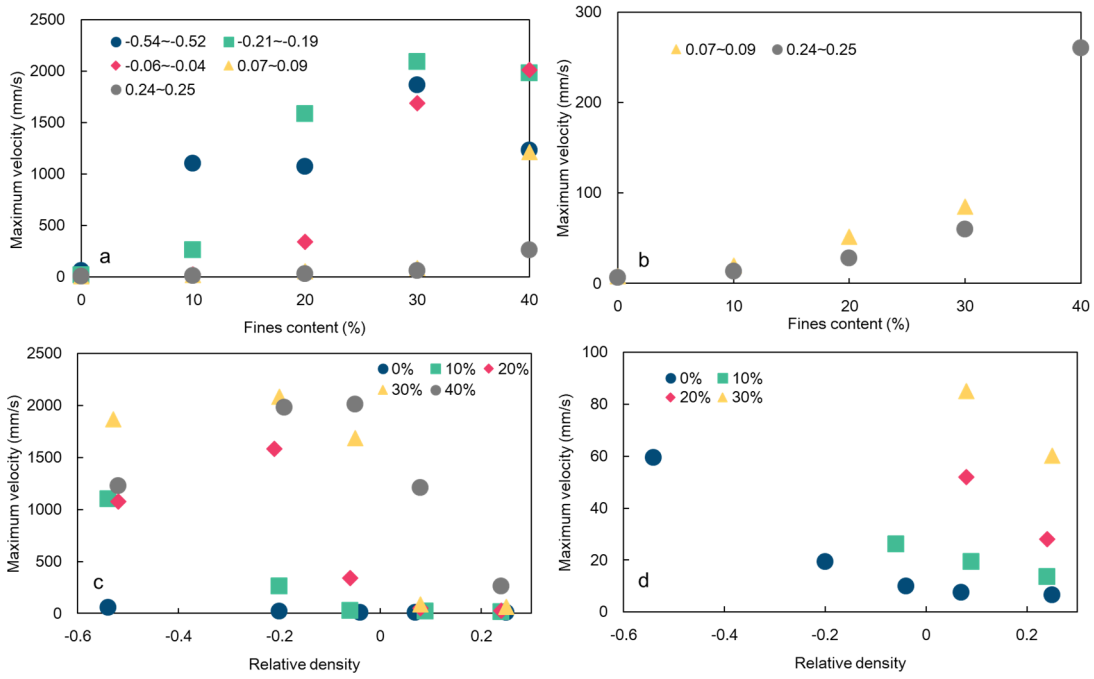

Fig. 16. (a) Fines content effects on maximum velocity of landslides with different relative densities. (b) Detailed information of fines content effects on maximum velocity of landslides with relative density of 0.07 ~ 0.09 and 0.24 ~ 0.25, which is enlarge part of Fig. 16a. (c) Relative density effects on maximum velocity of landslides with different fines content. (d) Detailed low velocity information of relative density effects on maximum velocity of landslides with fines content, which is enlarge part of Fig. 16c.

4.3 Fines content and relative density effects on pore water pressure built-up

Pore water pressure plays a significant role in the initiation and movement of landslides (Terzaghi, 1950). In experimental landslides illustrated by flume tests, many researchers showed high pore pressures generation at the base of flume occurred after instability and during the motion of landslide, rather than prior to sliding (Eckersley, 1990; Hu et al., 2018a, 2017; Moriwaki et al., 2004; Olivares and Damiano, 2007; Spence and Guymer, 1997; Wang and Sassa, 2003, 2001; X. Zhang et al., 2020). Okura et al. (2002) showed that excess pore water pressure generated in compressed and saturated sections by flume experiments. Ochiai et al. (2004) pointed out that a rapid increase in pore water pressure almost coincided with first observation of strain on the sliding surface by conducting a rainfall-induced landslide experiment on an outdoor natural slope. Moriwaki et al. (2004) performed a full-scale landslide

experiment, showing that pore water pressure in the upper soil slope increased due to the collapse of loose soil structure at shearing progress, while in the lower section of the slope, increasing of pore water pressure resulted from compression deformation and soil structure collapse by shearing. In this study, pore water pressure variation pattern both at bottom and within soil mass with soil mass tilting was summarized first according to all analyzing results of 25 flume tests (Fig. 17). As shown, in type 1 with slow individual sliding, PWP variation at bottom was divided into 2 classes: 1. PWP gradually increased first and slightly deceased, then a local built up occurred with soil tilting progress; 2. PWP gradually increased first and deceased later, the tilting of soil occurred after PWP reached the peak value. However PWP within soil mass showed different performance, the PWP was at the peak value when soil began to tilt. In type 3 with fast individual sliding, PWP sharply dropped when soil sudden to tilt or local build up after soil began to rotate. For PWP in the inner soil mass, a built up of PWP was observed after rotation of soil mass, which could be also captured in the type 4 with fast deep overall sliding and type 5 with fast shallow overall sliding. In the type 4 and type 5, PWP at bottom gradually increased first and then sharply decreased with soil tilting, or gradually increased first and then fluctuated (little decreasing and local built up), last dramatically declined with soil tilting.

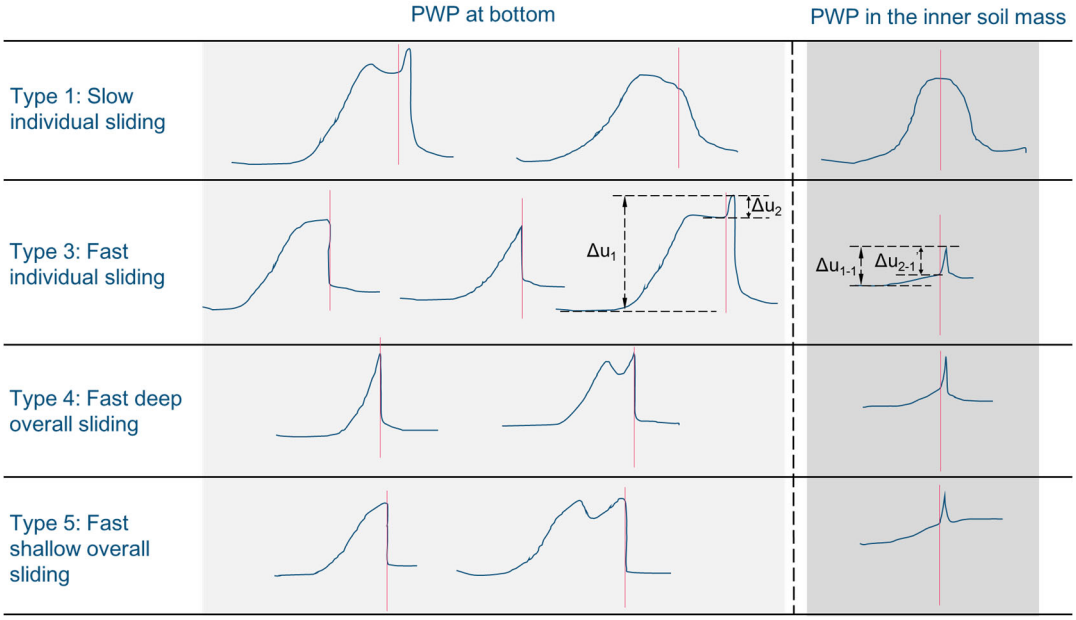

Fig. 17. Summarized pore water pressure variation pattern corresponding to soil mass tilting in each sliding mode including type 1, type 3, type 4 and 5. Δu_1, built-up of pore water pressure at bottom from initial value to peak value. Δu_2, local built-up of pore water pressure at bottom from lower value to peak value. $\Delta u_{1\text{-}1}$, built-up of pore water pressure in the inner soil mass from initial value to peak value. $\Delta u_{2\text{-}1}$, local built-up of pore water pressure in the inner soil mass from lower value to peak value. Red line shows the tilting initiation of soil mass.

Many scientists clearly illustrated the built up of pore water pressure in the soil mass by using landslide modeling (Eckersley, 1990; Hisada and Nakata, 2016; Hu et al., 2018, 2017; Olivares and Damiano, 2007; Tang et al., 2020; Wang and Sassa, 2003, 2001; Zhang et al., 2020). Among these results, Wang and Sassa (2003) found no obvious differences in pore water pressure build up in the mixtures with different fine loess content from limited test numbers. Hu (2017) identified an evident positive correlation between the peak PWP magnitude and the content of fine particles from 0% to 12%. Hisada and Nakata (2016) found the built-up of pore water pressure overall increased with fines content increasing from 5% to 25% at the

same rainfall intensity. Different results obtained by previous scientists may resulted from various fine particles content range or fines sorts. In this study, to examine the pore water pressure reaction with fine particles content, two types of PWP reaction at bottom of P6 location and P7 location (Fig. 4) were used. The first is peak PWP magnitude at bottom from initial value to peak value Δu_1, the second is built-up of pore water pressure at bottom from local lower value to peak value Δu_2 (Fig. 17), corresponding PWP in the inner soil mass was termed as $\Delta u_{1\text{-}1}$ and $\Delta u_{2\text{-}1}$ (Fig. 17). For the peak magnitude of pore water pressure from initial value to peak value, the maximum of peak PWP magnitude at P6 location was collected from the those at bottom and within soil mass, which was termed as $p6_{max\text{-}1}$ (maximum of Δu_1 and $\Delta u_{1\text{-}1}$ of P6 location), correspondingly, the maximum of peak PWP magnitude at P7 location was collected from the value at bottom and within soil mass, which was termed as $p7_{max\text{-}1}$ (maximum of Δu_1 and $\Delta u_{1\text{-}1}$ of P7 location). On the other hand, for the built-up of pore water pressure from local lower value to peak value, the maximum of local PWP build-up at P6 location was collected from those at bottom and within soil mass, which was termed as $p6_{max\text{-}2}$ (maximum of Δu_2 and $\Delta u_{2\text{-}1}$ of P6 location), correspondingly, the maximum of local PWP build-up at P7 location was also termed as $p7_{max\text{-}2}$ (maximum of Δu_2 and $\Delta u_{2\text{-}1}$ of P7 location). In landslide type of overall sliding, the PWP sensors both at P6 and P7 location were simultaneously involved in the landslide progress, then the maximum of $p6_{max\text{-}1}$ and $p7_{max\text{-}1}$, and maximum of $p6_{max\text{-}2}$ and $p7_{max\text{-}2}$ were collected to illustrate typical PWP reactions. In landslide type of retrogressive individual sliding, PWP sensors at P6 and P7 location were successively involved in the landslide progress, here we focused on the collected PWP value of $p6_{max\text{-}1}$ and $p6_{max\text{-}2}$ to illustrate typical PWP reactions. The two types of PWP reactions based on peak PWP magnitude from initial value to peak value and built-up of pore water pressure from local lower value to peak value were divided to discuss (Fig. 18). Fig. 18a shows the fines content effects on peak PWP magnitude from initial to peak on samples with different relative densities, as shown, no clear tendency was observed of peak PWP magnitude with increased fines content at different relative densities. Fig. 18b shows relative density effects on peak PWP magnitude on samples with different fines content, as shown no clear relationship was observed between peak PWP magnitude and increased fines content at different relative densities. Fig. 18c shows fines content effects on pore water pressure built-up from local lower to peak on samples with different relative densities. As shown, an overall fluctuation tendency was observed, the PWP build up increased when fines content increased to 10%, and decreased with fines content increased to 20%, then build-up of PWP increased again with fines reached to 30% content, last the build-up of PWP declined when fines content is 40%, here we could observed two optimal fines contents contributing to the PWP build up, which is 10% and 30% respectively. Fig. 18d shows relative density effects on pore water pressure built-up from local lower to peak on samples with different fines content. As shown, a clear overall tendency could be observed, build-up of PWP slightly increased with relative density increased from -0.06 to -0.04, but when relative density beyond -0.04, reverse tendency occurred, showing significant drop with further relative density increasing, here a threshold for relative density around -0.04 between -0.2 and 0 could be identified to mark a transition from increasing to decreasing of PWP built up, contributing to the greatest build-up of PWP.

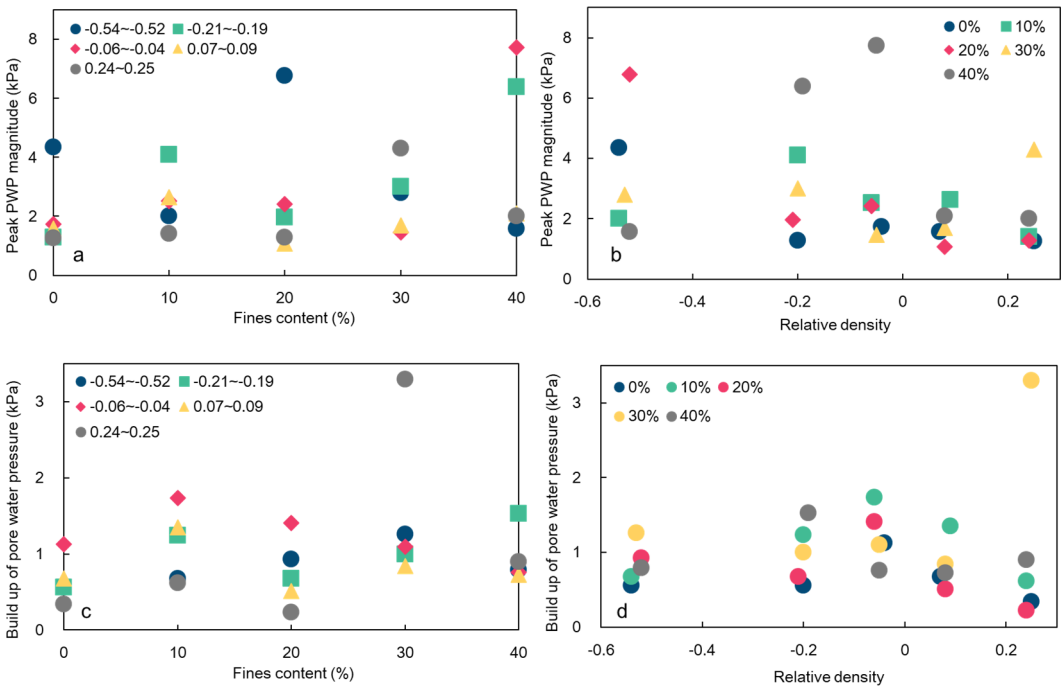

Fig. 18. (a) Fines content effects on peak PWP magnitude from initial to peak on samples with different relative densities. (b) Relative density effects on peak PWP magnitude from initial to peak on samples with different fines content. (c) Fines content effects on pore water pressure built-up from local lower to peak on samples with different relative densities. (d) Relative density effects on pore water pressure built-up from local lower to peak on samples with different fines content. Peak PWP magnitude was collected by following method, overall sliding: ($p6_{max-1}$, $p7_{max-1}$) –max, retrogressive individual sliding: $p6_{max-1}$, ($p6_{max-1}$, $p7_{max-1}$) – max: maximum of $p6_{max-1}$ and $p7_{max-1}$, $p6_{max-1}$/$p7_{max-1}$: maximum of Δu_1 and Δu_{1-1} of P6/P7 location. Build-up of pore water pressure collected by following method, overall sliding: ($p6_{max-2}$, $p7_{max-2}$) –max, retrogressive individual sliding: $p6_{max-2}$, ($p6_{max-2}$, $p7_{max-2}$) – max: maximum of $p6_{max-2}$ and $p7_{max-2}$, $p6_{max-2}$/ $p7_{max-2}$: maximum of Δu_2 and Δu_{2-1} of P6/P7 location.

4.4 Effect factor, assessing index considering fines content and fines effect mechanism proposed

4.4.1 Equivalent granular void ratio index comparing void ratio

Different factors and assessing indexes were used to evaluate and explain the behavior of granular soils. Among them, relative density or void ratio was found to be a key state variable for predicting the static liquefaction behavior of soils based on laboratory element tests including drained and undrained static triaxial compression tests (Sabbar et al., 2017; Yamamuro and Lade, 1997). Through flume tests, Wang and Sassa (2001) revealed that there was an optimal initial density for pore water pressure build up, in which motion velocity and transport distance were greatest. Zhang et al. (2020) highlighted that relative density effects on the progressive sliding and sudden collapse of tailing deposits by serials flume tests, and identified an optimal relative density of 0.35 contributing to the peak sliding velocity in landsliding progress using tailing dam materials. However, void ratio may not be an effective and appropriate variable for characterizing sand with fines under critical state soil mechanics framework, the evaluation of how fines content affect the mechanical behavior of granular soils has been one of the interesting subjects in geological community due to the inability of global void ratio (e) to entirely assess the actual fines content effects (Chen et al., 2020; Porcino et al., 2021; Porcino and Diano, 2017; Rahman et al., 2008; Rahmani and Abolhasan Naeini, 2020). The concept of intergranular void ratio (e_s) and

interfine void ration (e_f) were proposed to interpret the behavior of mixtures with silty sand (Thevanayagam, 1998; Thevanayagam and Mohan, 2000). These two concepts are defined as follows:

$$e_s = \frac{e+(FC/100)}{1-(FC/100)} \quad (1)$$

$$e_f = \frac{e}{FC/100} \quad (2)$$

Where e is the global void ratio, FC is the fines content. At low fines content less than the threshold value, the definition of intergranular void ratio, e_s, is based on the assumption that all of the fines in sand-fine mixtures can be approximated as void, their contribution to the force structure can be neglected. If the fines content (FC) exceeds the threshold, the soil becomes governed by the contacts between the fines, whereas the coarser grains float within the finer-grains matrix, then interfine void ratio, e_f, was used.

However, in the case of low fines content, with an increase in fines content, the role of the fines in the force chain should not be fully ignored, since some portion of fines may come in between the contact of sand grains and participate in the force structure due to the movement and sliding of soils under shearing. Similarly, at high fines content, the reinforcement effect by the coarse grains also be introduced. To take such mechanisms into account, new equivalent intergranular void ratio (e_s*) and equivalent interfine void ratio e_f* were derived from the modification in intergranular void ratio (e_s) and interfine void ratio (e_f) (Thevanayagam et al., 2002):

$$e_s^* = \frac{e+(1-b)(\frac{FC}{100})}{1-(1-b)(\frac{FC}{100})} \quad (3)$$

$$e_f^* = \frac{e}{\frac{FC}{100}+\frac{1-FC/100}{R_d^m}} \quad (4)$$

Where e is the void ratio, FC is the fines content, b is the fraction of fines that actively participates in the force structure. $R_d = D_{50}/d_{50}$ = size disparity ratio, $0 < m < 1$ and m = coefficient that depends on grain characteristics and fine grain packing (Kanagalingam and Thevanayagam, 2005; Thevanayagam, 2007a, 2007b). In the mixtures with fine content less than threshold, the mechanical behavior is primarily affected by the coarser particles contact, and fine grains have a secondary role in the transfer of inter-grain forces. However, once fine content increases beyond the threshold, the behavior of mixtures is controlled significantly by fine-grains contacts, and the role of gravel particles becomes less important and therefore the opposite trend was observed.

In the new equivalent intergranular contact void ratios theory framework, the determination of two parameters threshold fines content (FC_{th}) and fraction of fines that actively participates in the force structure (b) is significant (Barnett et al., 2020; C. S. Chang et al., 2021; Chang and Deng, 2019; Mohammadi and Qadimi, 2015; Ni et al., 2004; Porcino et al., 2021; Rahman et al., 2011, 2008). Threshold fines content (FC_{th}), also termed ‘‘limiting fines content’’ or ‘‘transitional fines content’’, is the specific value of the fines content at which the way the fines influence the behavioral properties of the mixture is reversed, has been introduced to distinguish the regime of fines in coarse (coarse-material-dominated behavior) from coarse in fines (fines-material-dominated behavior) soil mixtures (Rahman et al., 2011, 2008; Thevanayagam et al., 2002). There are different methods to determine the fine content thresholds in binary packing system. One approach is to use laboratory test indices: maximum void ratio (e_{max}) and minimum void ratio (e_{min}), the fine content percentage, in which e_{max} and e_{min} are minimum, is the fine content threshold (Lade et al., 1998; Porcino and Diano, 2017; Rahmani and Abolhasan Naeini,

2020; Yang and Wei, 2012; Zuo and Baudet, 2020, 2015). Variation results of index void ratios with silt content, shown in Figure 3b, highlight a transitional behavior, with FC_{th} around 30~40%, the value of maximum void ratio (e_{max}) reaches its lowest point at 30% fines content, which is earlier than minimum void ratio (e_{min}) reaching lowest point at 40% fine content, though e_{min} decreases at a faster rate before reaching FC_{th}. In another approach, the FC_{th} can be determined by the empirical equation developed by Rahman et al. (2009), which has been evaluated by Mohammadi and Qadimi (2015), Rahman and Sitharam (2020) and Chen et al. (2020), as below:

$$FC_{th} = 0.40 \times \left(\frac{1}{1+e^{\alpha-\beta\chi}} + \frac{1}{\chi}\right) \quad (5)$$

Where α=0.50 and β=0.13 are curve-fitting constants; and χ is the particle-size disparity ratio, $\chi=D_{10}/d_{50}$. The application of Eq. (5) to the mixtures tested in present study provides a value of FC_{th} = 32% being approximately consistent with the experimental values between 30% and 40% of index void ratios and experimental flume tests results.

The parameter, b, represents the fraction of fines active in force structure of the soil skeleton, the value of it can be determined by semi-empirical equation proposed by Rahman and Lo (2008) , as below:

$$b = \left[1 - \exp\left(-0.3 \times \frac{FC/FC_{th}}{k}\right)\right] \times \left(r\frac{FC}{FC_{th}}\right)^{r} \quad (6)$$

This equation for b has been evaluated with various emerging datasets and further been simplified to the new equation proposed by Mohammadi and Qadimi (2015).

$$b = \left[1 - \exp\left(-\frac{0.3}{k}\right)\right] \times \left(r\frac{FC}{FC_{th}}\right)^{r} \quad (7)$$

Where r=1/χ and k=1-$r^{0.25}$.

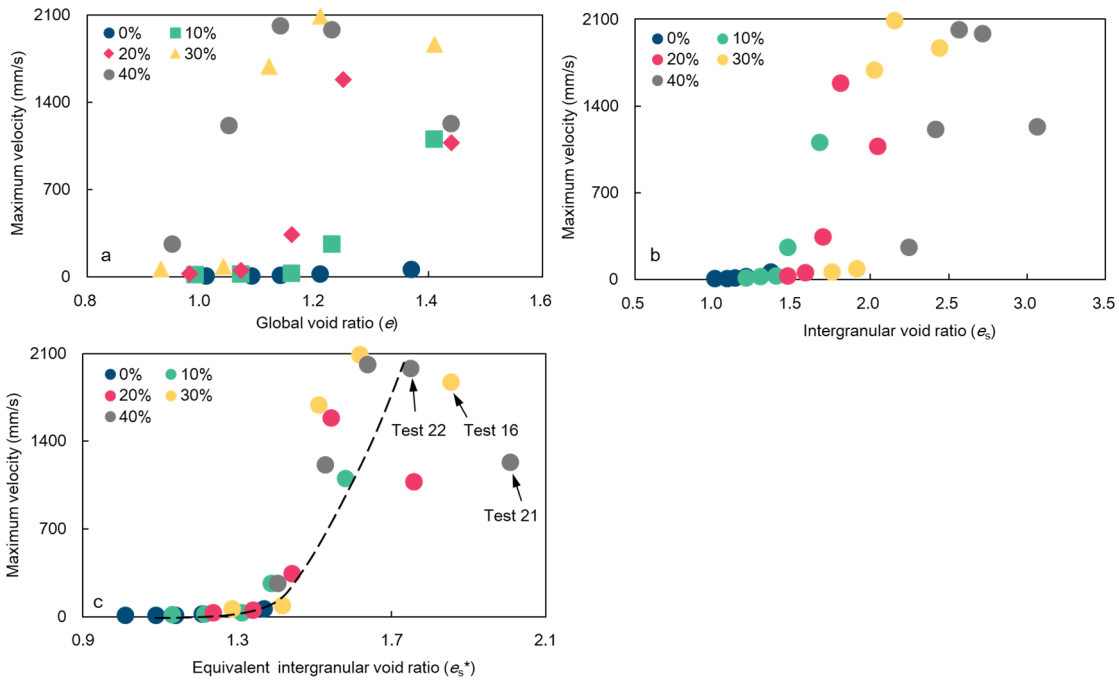

Fig. 19. (a) Maximum velocity variation against global void ratio (e) of mixtures with different fines content. (b) Maximum velocity variation against intergranular void ratio (e_s) of mixtures with different fines content. (c) Maximum velocity variation against equivalent intergranular void ratio (e_s^*) of mixtures with different fines content.

Figure 19 reveals the maximum velocity variation versus different assessing indices including global void ratio (e), intergranular void ratio (e_s) and equivalent intergranular void ratio (e_s*). As shown in Figure 19a, maximum velocity increased with void ratio increasing at 10% fines content. When the mixture was at 20%, 30% and 40% fines content condition respectively, a certain optimal void ratio was observed in the each condition, the maximum velocity increased with increased void ratio until reached to a certain value, and then decreased when beyond this certain value, however, no obvious overall tendency was observed between velocity and void ratio in all mixtures considering different fines content, indicating void ratio (e) index may not be an effective and appropriate variable for characterizing sand with fines. Similarly, as shown in Figure 19b, no obvious overall tendency was observed between velocity and intergranular void ratio (e_s) in all mixtures considering different fines content, indicating intergranular void ratio index (e_s) also could not be a suitable variable for characterizing sand with fines. However, in Figure 19c, a clear overall tendency was observed, the maximum velocity first slightly increased with increased equivalent intergranular void ratio (e_s*) to 1.3 and rapidly increased with further equivalent intergranular void ratio. Here we need to notice that the maximum velocity started to show decreasing tendency with equivalent intergranular void ratio (e_s*) beyond 1.7. In this range, the maximum velocity showed slight declination when mixture has 30% fines content (test 16), the maximum velocity dropped very small first (test 22) but dropped sharply with further increasing equivalent intergranular void ratio (test 21) when fines content was at 40%. Referring to the observed results of Figure 15a, the landslide phenomena of these tests has shallow overall sliding events, which was assigned into type 5, and calculated threshold fines content was at 30%-40%, we could conclude that maximum velocity began to decrease with further equivalent intergranular void ratio because of the mixtures of these testes was in a transition state associating with density, which transforms from coarse particles dominating and fine particles participating to fine particles dominating and coarse particles participating. Especially, velocity dropped sharply with further increasing equivalent intergranular void ratio in test 21 with 40% fines content, indicating the fine particles has begun to control the mixture behavior, and the coarse grains played a secondary role. This transition is associated with mixture density though fines content is high. If the mixture with 40% fines content is dense, coarse grains play a dominate role in the behavior, fine particles play a secondary role. However, if this mixture is loose at the same fines content (40%) (test 21), the fine grains separated the contact of coarse particles, the mixture behavior is dominated by fines contact, thus the transition state occurred. This phenomenon could easily occur at high fines content around threshold fines content (FC_{th}), if fine content is low, coarse particles could play a first role both in dense and loose mixtures.

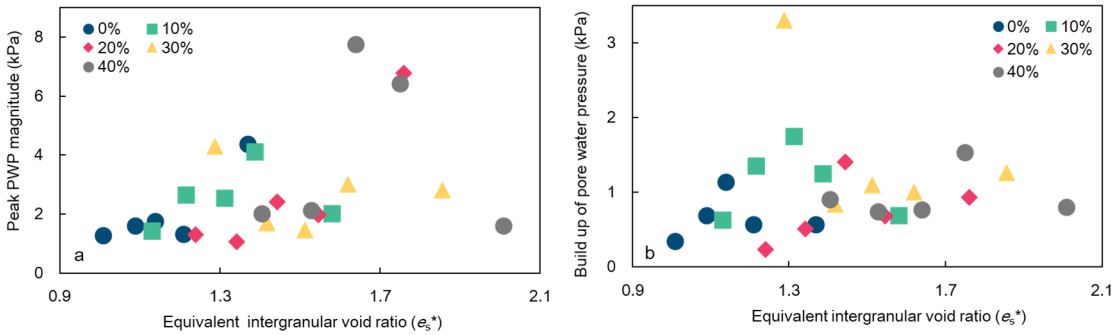

Fig. 20. (a) Peak PWP magnitude variation against equivalent intergranular void ratio (e_s^*) of mixtures with different fines content. (b) Build-up of PWP against equivalent intergranular void ratio (e_s^*) of mixtures with different fines content.

Figure 20 illustrates pore water pressure variation against equivalent intergranular void ratio. As shown in Figure 20a, no clear overall relationship was observed between peak PWP magnitude and increased equivalent intergranular void ratio at different fines content. As shown in Figure 20b, an overall fluctuation trend with bimodal pattern was observed between build-up of PWP and increased equivalent intergranular void ratio. PWP build up gradually increased with equivalent intergranular void ratio increasing to around 1.3, and then declined with further equivalent intergranular void ratio increasing from 1.3 to 1.6, last showed a fluctuation again when equivalent intergranular void ratio beyond 1.6. An optimal equivalent intergranular void ratio of 1.3 at the range of 0.9-1.6 was clarified to contributing to maximum build-up of PWP. The second fluctuation of build-up of PWP when equivalent intergranular void ratio beyond 1.6 resulted from the transition mechanism from coarse particles dominating and fine particles participating to fine particles dominating and coarse particles participating. Comparing to the velocity results of Figure 19c and PWP results of Figure 20, we could see the motion of landslide mass consisted of mixtures with high amount of fines was not only depended on pore water pressure but also depended on the fine particle itself, which further indicates fine content affects the movement of landsliding mass not only through fine particles effects on pore water pressure generation, but also through fine particles themselves, the deeper effect mechanism are needed to be reveal.

4.4.2 Conceptual mixture model proposed and fines affecting mechanism.

Here, as shown above, non-plastic fines could play a significant role in the initiation and movement of landslides consisted of mixtures with amounts of fine grains, however the fines effects mechanism is complex. Many researchers focused on the fines effect mechanism. Grains in the silt-clay fraction could remain suspended and act as part of fluid (Iverson, 1997), and high PWP may dissipate slowly in rapid landslides that contain fines, the moving materials consequently could remain highly mobile (Iverson et al., 2015). Okada and Ochiai (2008) also pointed out the generation of excess pore pressure resulted from fine grains suspension in the pore fluid and low permeability of the mixture in the moving granular slow mass by using mixtures with pumiceous gravel and volcanic ash. Nishiguchi and Uchida (2022) suggested that fine sediments could behave as part of interstitial fluid in progress of debris flow, and some fine sediments were stored into void space of the riverbed during debris flow deposition. Wang and Sassa (2003) argued that generated PWP maintaining mechanism was the flotation of fine grains and PWP increasing supporting grains suspension in the pore liquid during the movement of mixtures with high fines content. Hu et al. (2017) identified an evident positive correlation between the PWP peak value and the fine particles content range from 0% to 12%. Hisada and Nakata (2016) found the built-up of pore water pressure overall increased with fines content increasing from 5% to 25% at the same rainfall intensity. Furuya et al. (1999) pointed out that the fine particles can be eroded and transported by surrounding groundwater flows, resulting in enlarge voids and increasing susceptibility to failure of the landslide mass. However, Hu et al. (2018) demonstrated internally erodible small grains play a major role in producing grain coarsening and then triggering unstable, failure and fluidization of the granular mass through experiments on loose artificial landslide modeling. Besides fine particles effect on PWP generation, HSÜ (1975) hypothesized that the fine-grained matrix itself could fluidize the coarser materials and move debris with absent of supporting fluid. Perinotto et al. (2015) pointed out that the presence of fine-grained matrix could diminish the collision rate between coarser grains, partially inhibit the dynamic fragmentation of granular mass, they identified a grinding limit of 500 μm in the natural debris avalanche, in which the < 500 μm fraction acts as an interstitial granular fluid of rounded grains facilitating debris avalanche movement, these fine-grained particles (interstitial fluid) can locally

decrease the effective normal pressure on larger particles, consequently reduce bulk frictional resistance and fluidize the granular materials. The addition of fines into coarse-grained particles changes the internal microstructure pattern of matrix, fine-grains behave as a lubricant when they occupy contact locations between coarse-grains, consequently reducing strong contacts between coarse particles (Rahmani and Abolhasan Naeini, 2020, Hyodo et al., 2017). These ideas are supported by our findings of this study. Some landslides composed of high fines content are characterized by suddenly initiation and rapid movement without high peak PWP magnitude and high build-up of PWP (Figures 16 and 18). Clear tendency could be observed of fines content and density index effects on landslide motion, however, corresponding PWP variation trend is not obvious with fluctuation, meaning the generated PWP variation including peak PWP magnitude and build-up of PWP did not well matched the landslide mobility variation (Figure19c and Figures 20a, 20b), but still fines have effects on generating pore water pressure (Figures 18 and 20). Based on these results, here we could conclude that the fines content affects the initiation and movement of landslide not only through generated pore water pressure partially contributing to sliding mass rapid motion as well as fine particles themselves facilitating highly mobility of landslide.

Based on the framework of intergranular void ratio, figure 21 presents the microstructure conceptual mixture model to interpret the mechanisms controlling the landslide behavior of sliding mass with different amounts of fines content and different densities. When the mixture density is low (loose state), for mixture with a small amount of fine particles, fines are entirely located into the void space between coarse-grained materials, playing only a filler role (state 2), which does not participate in force chain delivery. With an increase in fine grains content, fine grains partially come in between the strong contact of coarse particles, and some fines actively participate in the force structure (state 3). In these states, fine-grains content is less than threshold, the mechanical behavior of mixture is primarily affected by coarse grains contact, and fine particles behave a secondary role in grain force transferring. However, when fine particles content is higher and increases reach the threshold, fines separate and disperse the contacts of coarse grains, the mechanical behavior of mixtures is dominated significantly by fine particles contacts (state 4), and the role of coarse grains diminish, fines primarily participate in the transfer of forcing chain. The force chain transfer structure of mixture could change with mixture density increasing. As shown in Figure 2, if the mixture density is high (dense state to the opposite loose state), thought at the same high fines content around threshold, structure of mixture could transform form fines primarily controlling and coarse particles participating (state 4) to coarse grains dominating and fine grains participating (state 3 or state 6). This is the mechanism of landslide types transfer and landslide maximum velocity varying a lot when fines content is at high fraction though around threshold, especially in test 16, test 21 and test 22 (Figures 15, 16 and 19).

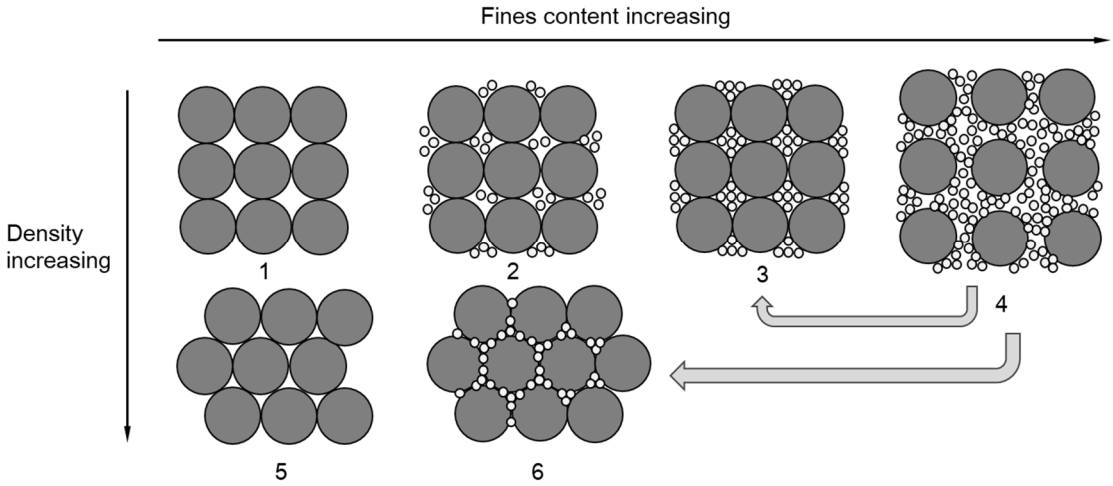

Fig. 21. Conceptual mixture model interpreting the mechanisms that control the landslide behavior of sliding mass with different amounts of fines content and different densities. States from 1 to 4 show microstructure of mixture with fines content increasing at lower density, states from 5 to 6 show microstructure of mixture with fines content increasing at higher density.

4.5 Precursory events at catastrophic sliding, and tilting is prior to sliding of mass

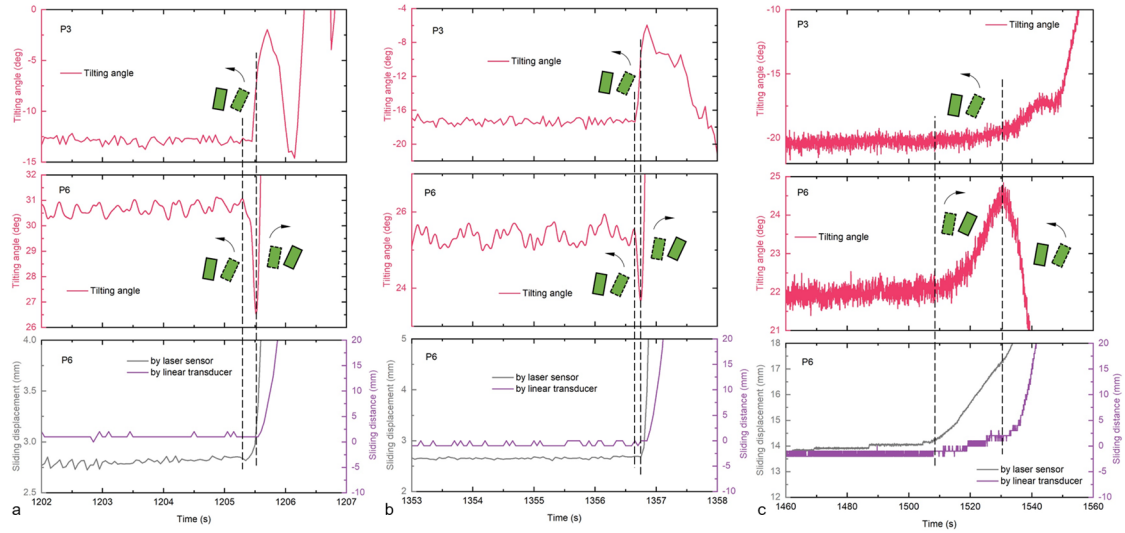

Fig. 22. Precursory events before catastrophic landslide, and tilting is prior to sliding. (a) Results of tilting angle variation at P3 location, bottom of P6 location, and sliding displacements measured by laser sensor and linear transducer in test 11. (b) Results of tilting angle variation at P3 location, bottom of P6 location, and sliding displacements measured by laser sensor and linear transducer in test 6. (c) Results of tilting angle variation at P3 location, bottom of P6 location, and sliding displacements measured by laser sensor and linear transducer in test 2.

Our study showed the fines content played a significant role in the landslide type, mainly including slow moving landslide and fast catastrophic landslide with fluidized motion. Fluidized landslide evolving into rapid and destructive fluid-like motion are hardly predictable since sudden initiation with little warning and accelerating dramatically of these landslides. Many researchers captured precursory signals before clarified landslide occurring by using vibrations (micro seismicity) and sounds (acoustic emissions) methods with accelerometers and acoustic sensors (Hu et al., 2018b). In our study, some important precursory events were captured by subsurface tilting sensor. It would be noted that for tilting sensor at P3 location, the tilting angle showed a decreasing curve from the initial degree to certain degree

with clockwise rotation of tiltmeter when the flume was lifted from horizon to 25°, so the tilting angle increases when tiltmeter at P3 location anticlockwise rotates. For tilting sensor at bottom of P6 location, the tilting angle showed an increasing curve from the initial degree to certain degree with clockwise rotation of tiltmeter when the flume was lifted from horizon to 25°, so the tilting angle shows decreasing tendency when tiltmeter at P6 location bottom anticlockwise rotates. Figure 22 shows the results of subsurface titling angle variation at P3 location, bottom of P6 location, and corresponding sliding displacements at bottom of P6 location measured by laser sensor and linear transducer in test 11, test 6 and test 2. As shown in figure 22a, in the catastrophic landslide in test 11, tiltmeter at bottom of P6 location first began to rapidly anticlockwise rotate at 1205.3 s, accompanied by increasing micro sliding displacement of ball at the same location captured by laser sensor, 0.2 s later, the tiltmeter suddenly changed to rotate clockwise at 1205.5 s, this change in tiltmeter rotation coincided with a sharp increase in macroscopic sliding distance of ball at the same location measured by linear transducer. Divergence of tilts was observed at different depths, tiltmeter at P3 location measured vertically suddenly anticlockwise rotated at 1205.3 s and 1205.5 s, and continued to same rotation with no changing rotation direction in the short periods. Here a precursory events exhibited by tiltmeter at the bottom P6 location could be observed before macroscopic sliding of matter, accompanied by sudden and dramatic changing of rotating direction. As shown in figure 22b, in the catastrophic landslide in test 6, tiltmeter at bottom of P6 location suddenly anticlockwise rotated at 1356.65 s, accompanied by suddenly increasing tilting angle of tiltmeter at P3 location measured vertically, 0.1 s later, the tiltmeter at bottom P6 location suddenly changed to rotate clockwise at 1356.75 s, this change in tiltmeter rotation coincided with a sharp increase in microscopic sliding displacement of ball at the same location arrested by laser sensor, which is prior to the macroscopic sliding distance arrested by laser sensor. Here a significant precursory events exhibited by tiltmeter at the bottom P6 location could be observed prior to both micro and macroscopic sliding of mass, accompanied by sudden and dramatic changing of rotating direction. This kind of phenomena were also could be observed in previous showed test such as test 23 (figure 12d), and some testes (test 12 and test 17) illustrated the rapid rotation of tiltmeter at bottom of P6 location coincided with sharp increase both in micro and macroscopic sliding of mass (figure 11b and figure 12b). Similar divergence of subsurface tilts at different depths and its sequence with surface displacement in the rapid catastrophic landslide exhibited in flume tests were detail discussed by Iverson et al. (2000). They illustrated us the tilting sensor at all depths rotated slightly upslope (anticlockwise rotation) from 2781 to 2781.5 s in a landslide modeling test with loose soil, after 2781.5 s, divergence of subsurface tilts occurred, tiltmeters at deep depths changed to rotate rapidly downslope (clockwise rotation) attributed to drag due to the translation sliding along the constructed concrete bed, on the contrast, tiltmeters near surface showed accelerated upslope rotation without changing rotation direction (continuing anticlockwise rotation) resulted from superincumbent rotational landsliding, and the change in rotation of deep tiltmeters was accompanied by rapid accelerating in surface displacement.

Although very similar phenomena were both observed in our tests and their tests, some differences are summarized in our tests: 1, in this study, tilting variation was mainly compared with corresponding inner displacement using small ball placed in the inner soil mass at the same location (bottom at P6 location), while Iverson et al. (2000) compared the subsurface tilts and surface displacement. 2. Iverson et al. (2000) showed that the change in rotation of deep tiltmeters at 2781.5 s was accompanied by rapid accelerating increase in surface displacement, during previous 0.5 s, all tiltmeters rotated slightly upslope accompanied by gentle increasing surface displacement, which indicates the entire rotation progress is consistent with the surface displacement development, further showing the periods from the initiation of

rotation (2781 s) to change of rotation (2781.5 s) was accompanied by slowly increasing of surface displacement. However, our results illustrated the change in rotation of tiltmeters at bottom of P6 was accompanied by initial increase in macroscopic sliding distance (figure 22a) even in microscopic sliding displacement (figure 22b), suggesting the periods from the initiation of rotation to change of rotation was prior to macroscopic displacement even microscopic sliding displacement of soil mass, which is different from the findings in Iverson et al. (2000). 3. Iverson et al. (2000) produced the rapid catastrophic landslide in landslide experiments by loose soil with initial porosity 0.52, in the test, the obvious visible soil compaction by wetting (namely settlement) was reported, evidenced by the slight downslope rotation of tilting sensors at all depths. This similar visible settlement was also captured in our tests with fast shallow overall sliding in type 5 using loose sample, which also measured by tiltmeters (figure 13a and figure 8c). In this types of landslide, the obvious visible settlement to be easily identified could be regarded as one of the precursory events before the occurring of fast sliding. However, in our study, besides fast shallow overall sliding in type 5, we more produced fast individual sliding in type 3 and fast deep overall sliding in type 4 by using denser samples, in these tests, no visible settlement was observed and no tilting variation captured by tiltmeter in the early stage (figure 12), the displacements and tilting angle curve nearly keep the certain constant before the initiation of rotation, it would be hard to identify the precursory signals. However, in these tests with denser samples, we found the periods from initiation of rotation to change of rotation was prior to macroscopic displacement even microscopic sliding displacement of soil mass, which could be an important and effective precursory event before the catastrophic sliding with denser samples though last in very short term (0.1 to 0.2 s in the tests).

The event that tilting is prior to sliding of mass not only occurred at fast moving landslide, but also could be observed at slow moving landslides. Figure 22c shows results of tilting angle variation at P3 location, bottom of P6 location, and sliding displacements measured by laser sensor and linear transducer in test 2. As shown, tiltmeter at bottom of P6 location first began to gradually clockwise rotate at about 1508 s, accompanied by gradual increasing micro sliding displacement of ball at the same location captured by laser sensor, 25 s later, the tiltmeter gradually changed to rotate anticlockwise at 1531 s, this change in tiltmeter rotation coincided with increase in macroscopic sliding distance of ball at the same location measured by linear transducer. Tiltmeter at P3 location measured vertically slightly anticlockwise rotated from 1508 s and 1531 s, and continued to same rotation with no changing rotation direction in the short periods. In this test, we could observe the periods from initiation of rotation to change of rotation was prior to macroscopic displacement of soil mass, which is similar with the phenomenon showed in Figure 9. This phenomena was observed in the recent field investigation with natural landslide events. Doi et al. (2020) showed the observation results of a coastal Shirishizu landslide in Hokkaido. They showed that inclination variation occurred at least 1month prior to the landslide displacement, which resulted from coastal erosion, they also found tilting angle accelerating variation at around 12:00 on 1 March 2018 is prior to the landslide displacement at the backscarp, although these sensors were placed at different locations of landslide. Our results could provide the laboratory evidence for this phenomenon occurred in natural landslide events.

5. Conclusions

In this research, in order to clarify the effect of non-plastic fines content on the initiation and movement of rainfall-induced landslides, 25 laboratory flume tests have been performed using mixtures of silica sand and non-plastic fines containing different content of fines in dry weight with various densities at same fines content. Based on the results illustrated in this study, the following conclusions could be

drawn:

(1) Fines content plays a significant role in the failure mode and landslide type. the landslide mode illustrated a clear gradient variation trend with fines content increasing and relative density increasing. The landslide types were summarized as following: slow individual sliding in type 1 characterized by entire inconsistent retrogressive sliding behavior, sudden multiple sliding in type 2, fast individual sliding in type 3 characterized by entire inconsistent retrogressive sliding behavior, fast deep overall sliding in type 4 characterized by entire rapid flowslide motion with large volume and deep sliding surface, fast shallow overall sliding in type 5 with shallow sliding surface. The landslide mode could transfer from type 1 to type 5 with fines content increasing, and change from type 5 to type 1 with relative density increasing at high fines content.

(2) Different type landslides could be illustrated by soil rotation, pore water pressure reaction and soil mass sliding velocities. For soil rotation, the tilting angle gradually increased or decreased with landslide progress in type 1, but tilting angle sharply increased or decreased with the progress of sliding in types from 2 to 5. For sliding velocity, velocity fluctuated with landslide progress in type 1 and 2, but the landslide mass moved continually without deceleration within the visible range in the flume test, which accelerated continuously in types from 3 to 5.

(3) Fines content has great effects on the movements of landslides. At relative density of -0.54 ~ - 0.52 and -0.21 ~ -0.19, an optimal fines content of 30% was observed contributing to the maximum velocity of landslides. At relative density of -0.06 ~ -0.04, the maximum velocity increased in total with increased fines content. The maximum velocity showed a gradual growth tendency with increased fines content both at relative density of 0.07 ~ 0.09 and 0.24 ~ 0.25. Relative density has greatly affect the movements of landslides, when fines content is low at 0% and 10 %, the maximum velocity decreased with relative density increasing, but at high fines content (20%, 30% and 40%), the optimal relative density at around -0.2 ~ -0.04 was observed to contributing to the maximum velocity of landslides.

(4) Fines have effects on pore water pressure (PWP) built-up on samples with different relative densities. An overall fluctuation tendency was observed, two optimal fines contents of 10% and 30% respectively contributing to the PWP build up maximum. Relative density have effects on pore water pressure built-up on samples with different fines content, a clear overall tendency could be observed, build-up of PWP slightly increased with relative density increased from -0.06 to -0.04, but when relative density beyond -0.04, reverse tendency occurred, showing significant drop with further relative density increasing, thus a threshold for relative density around -0.04 between -0.2 and 0 could be identified to mark a transition from increasing to decreasing of PWP built up, contributing to the greatest build-up of PWP.

(5) Comparing global void ratio (e), equivalent intergranular void ratio (e_s*) could be selected as an index to evaluate and explain the behavior of granular soils taking account of fines content, and threshold fines content was found around 30%~40%. The maximum velocity first slightly increased with increased equivalent intergranular void ratio (e_s*) to 1.3 and rapidly increased with further equivalent intergranular void ratio. But the maximum velocity started to show decreasing tendency with equivalent intergranular void ratio (e_s*) beyond 1.7. In this range, the maximum velocity showed slight declination when mixture has 30% fines content, the maximum velocity dropped very small first but dropped sharply with further increasing equivalent intergranular void ratio when fines content was at 40%. These phenomena could be explained by grain scale microstructures of mixtures involved mechanisms, as following, for mixtures of fine-grains content is less than threshold, the mechanical behavior of mixture is primarily affected by coarse grains contact, with an increase in fine grains content, fine grains partially come in between the

strong contact of coarse particles, actively participating in the force structure. However, when fine particles content is higher and increases reach the threshold, fines begin to separate and disperse the contacts of coarse grains, the mechanical behavior of mixtures is dominated significantly by fine particles contacts. This force chain transfer structure of mixture could change with mixture density varying at the same fines content around threshold (30% and 40% fines content in this study). Structure of mixture could transform form coarse grains dominating (fine grains participating) at dense state to fines primarily controlling (coarse particles participating) at loose state with density decreasing at the same high fines content around threshold. Fines effect mechanisms on the imitation and movement of landsliding mass not only through fine particles effects on pore water pressure generation, but also through fine particles themselves.

(6) Short term (0.1 to 0.2 s in the tests) precursory events could be observed by soil tilting at catastrophic sliding of soil mass. At fast moving landslide, tiltmeter at bottom of P6 location suddenly and sharply anticlockwise rotate, tenths of a second later, the tiltmeter suddenly changed to clockwise rotate, accompanied by increasing macroscopic sliding distance measured by linear transducer or even micro sliding displacement captured by laser sensor. The periods from initiation of rotation to change of rotation is prior to macroscopic displacement even microscopic sliding displacement of soil mass, which could be an important and effective precursory event before the catastrophic sliding. In addition, the event that tilting is prior to macroscopic sliding of mass also could be observed at slow moving landslides.

Table 2. Test conditions and summarized data in all flume tests

Series no.	Test. no.	Sample	Dry density	Void ratio	Relative density	Landsliding velocity description	Landsliding depth description	Settlement description	Corresponding PWP sensors during major failure	Maximum velocity	Built up of PWP (peak-initial)	Built up of PWP (peak-local)
			ρ_d (g/cm^3)	e	D_r					mm/s	kPa	kPa
1	1	S7-0	1.11	1.37	-0.54	Slightly fast (overall)	Deep	No settlement	P6 bottom, P7 bottom	59.4	4.4	0.6
	2	S7-0	1.19	1.21	-0.20	Slow (individual)	Deep	No settlement	P6 bottom, P7 bottom	19.3	1.3	0.6
	3	S7-0	1.23	1.14	-0.04	Slow (individual)	Deep	No settlement	P6 bottom, P7 bottom	10	1.7	1.1
	4	S7-0	1.26	1.09	0.07	Slow (individual)	Deep	No settlement	P6 bottom, P7 bottom	7.6	1.6	0.7
	5	S7-0	1.31	1.01	0.25	Slow (individual)	Deep	No settlement	P6 middle, P7 middle	6.68	1.3	0.3
2	6	S7-1	1.09	1.41	-0.54	Fast (overall)	Deep	Obvious settlement	P6 bottom, P7 bottom	1101.5	2.0	0.7
	7	S7-1	1.18	1.23	-0.20	Slightly fast (overall)	Deep	No obvious settlement	P6 bottom, P7 bottom	260.3	4.1	1.2
	8	S7-1	1.22	1.16	-0.06	Slow (individual)	Deep	No settlement	P6 bottom, P7 bottom	26.1	2.5	1.7
	9	S7-1	1.27	1.07	0.09	Slow (individual)	Deep	No settlement	P6 bottom, P7 bottom	19.5	2.6	1.4
	10	S7-1	1.32	0.99	0.24	Slow (individual)	Deep	No settlement	P6 bottom, P7 bottom	13.54	1.4	0.6
3	11	S7-2	1.08	1.44	-0.52	Fast (overall)	Deep	Obvious settlement	P6 bottom, P7 bottom	1074.5	6.8	0.9
	12	S7-2	1.17	1.25	-0.21	Fast (individual)	Deep	No obvious settlement	P6 bottom, P7 bottom	1582	2.0	0.7
	13	S7-2	1.22	1.16	-0.06	Slightly fast (overall)	Deep	No settlement	P6 bottom, P7 bottom	340.3	2.4	1.4
	14	S7-2	1.27	1.07	0.08	Slow (individual)	Deep	No settlement	P6 bottom, P7 bottom	51.9	1.1	0.5
	15	S7-2	1.33	0.98	0.24	Slow (individual)	Shallow	No settlement	P6 bottom, P7 bottom	28.2	1.3	0.2

4	16	S7-3	1.09	1.41	-0.53	Fast (overall)	Shallow	Obvious settlement	P6 middle, P7 bottom	1868	2.8	1.3
	17	S7-3	1.19	1.21	-0.2	Fast (overall)	Deep	No obvious settlement	P6 bottom, P7 bottom	2088	3.0	1.0
	18	S7-3	1.24	1.12	-0.05	Fast (individual)	Deep	No obvious settlement	P6 bottom, P7 bottom	1688	1.5	1.1
	19	S7-3	1.29	1.04	0.08	Slow (individual)	Deep	No settlement	P6 bottom, P7 middle	85.1	1.7	0.8
	20	S7-3	1.36	0.93	0.25	Slow (individual)	Deep	No settlement	P6 bottom, P7 bottom	60.1	4.3	3.3
5	21	S7-4	1.08	1.44	-0.52	Fast (overall)	Shallow	Obvious settlement	P6 bottom, P7 bottom	1229.5	1.6	0.8
	22	S7-4	1.18	1.23	-0.19	Fast (overall)	Shallow	Obvious settlement	P6 middle, P7 bottom	1980	6.4	1.5
	23	S7-4	1.23	1.14	-0.05	Fast (individual)	Deep	No obvious settlement	P6 middle, P7 bottom	2011	7.7	0.8
	24	S7-4	1.28	1.05	0.08	Fast (individual)	Deep	No settlement	P6 bottom, P7 bottom	1210	2.1	0.7
	25	S7-4	1.35	0.95	0.24	Slow (individual)	Deep	No settlement	P6 bottom, P7 bottom	260.3	2.0	0.9

Acknowledgments

This study is supported by the New Exploratory Research Grant (NO. 2021H-04) from Disaster Prevention Research Institute, Kyoto University.

References

Amini, F., Qi, G.Z., 2000. Liquefaction Testing of Stratified Silty Sands. J. Geotech. Geoenvironmental Eng. 126, 208–217. https://doi.org/10.1061/(ASCE)1090-0241(2000)126:3(208)

Bahadori, H., Ghalandarzadeh, A., Towhata, I., 2008. Effect of non plastic silt on the anisotropic behavior of sand. Soils Found. 48, 531–545. https://doi.org/10.3208/sandf.48.531

Barnett, N., Rahman, M.M., Karim, M.R., Nguyen, H.B.K., Carraro, J.A.H., 2020. Equivalent state theory for mixtures of sand with non-plastic fines: a DEM investigation. Géotechnique. https://doi.org/10.1680/jgeot.19.p.103

Bryant, S.K., Take, W.A., Bowman, E.T., 2014. Observations of grain-scale interactions and simulation of dry granular flows in a large-scale flume. Can. Geotech. J. 52, 638–655. https://doi.org/10.1139/cgj-2013-0425

Castro, G., Poulos, S.J., 1977. Factors Affecting Liquefaction and Cyclic Mobility. J. Geotech. Eng. Div. 103, 501–516. https://doi.org/10.1061/AJGEB6.0000433

Chang, C.S., Deng, Y., 2019. Revisiting the concept of inter-granular void ratio in view of particle packing theory. Géotechnique Lett. 9, 121–129. https://doi.org/10.1680/jgele.18.00175

Chang, C.S., Deng, Y., Goudarzy, M., Rahman, M., Wichtmann, T., 2021. Discussion on Revisiting the concept of inter-granular void ratio in view of particle packing theory. Géotechnique Lett. 11, 1–11. https://doi.org/10.1680/jgele.20.00148

Chen, G., Wu, Q., Zhao, K., Shen, Z., Yang, J., 2020. A Binary Packing Material–Based Procedure for Evaluating Soil Liquefaction Triggering during Earthquakes. J. Geotech. Geoenvironmental Eng. 146, 04020040. https://doi.org/10.1061/(ASCE)GT.1943-5606.0002263

Chen, N.S., Zhou, W., Yang, C.L., Hu, G.S., Gao, Y.C., Han, D., 2010. The processes and mechanism of failure and debris flow initiation for gravel soil with different clay content. Geomorphology 121, 222–230. https://doi.org/https://doi.org/10.1016/j.geomorph.2010.04.017

Cui, S., Pei, X., Huang, R., 2017. Effects of geological and tectonic characteristics on the earthquake-triggered Daguangbao landslide, China. Landslides 15, 649–667. https://doi.org/10.1007/s10346-017-0899-3

Cui, Y. fei, Zhou, X. jun, Guo, C. xu, 2017. Experimental study on the moving characteristics of fine grains in wide grading unconsolidated soil under heavy rainfall. J. Mt. Sci. https://doi.org/10.1007/s11629-016-4303-x

Dash, H.K., Sitharam, T.G., 2009. Undrained Cyclic Pore Pressure Response of Sand–Silt Mixtures: Effect of Nonplastic Fines and Other Parameters. Geotech. Geol. Eng. 27, 501–517. https://doi.org/10.1007/s10706-009-9252-5

Davies, T.R., McSaveney, M.J., 2009. The role of rock fragmentation in the motion of large landslides. Eng. Geol. https://doi.org/10.1016/j.enggeo.2008.11.004

Davies, T.R., McSaveney, M.J., Hodgson, K.A., 1999. A fragmentation-spreading model for long-runout rock avalanches. Can. Geotech. J. 36, 1096–1110. https://doi.org/10.1139/cgj-36-6-1096

Dufresne, A., Dunning, S.A., 2017. Process dependence of grain size distributions in rock avalanche deposits. Landslides 14, 1555–1563. https://doi.org/10.1007/s10346-017-0806-y

Dufresne, A., Geertsema, M., Shugar, D.H., Koppes, M., Higman, B., Haeussler, P.J., Stark, C.,

Venditti, J.G., Bonno, D., Larsen, C., Gulick, S.P.S., McCall, N., Walton, M., Loso, M.G., Willis, M.J., 2018. Sedimentology and geomorphology of a large tsunamigenic landslide, Taan Fiord, Alaska. Sediment. Geol. 364, 302–318. https://doi.org/10.1016/j.sedgeo.2017.10.004

Dufresne, A., Prager, C., Bösmeier, A., 2016. Insights into rock avalanche emplacement processes from detailed morpho-lithological studies of the Tschirgant deposit (Tyrol, Austria). Earth Surf. Process. Landforms 41, 587–602. https://doi.org/10.1002/esp.3847

Eckersley, D., 1990. Instrumented laboratory flowslides. Géotechnique 40, 489–502. https://doi.org/10.1680/geot.1990.40.3.489

Fan, X., Scaringi, G., Korup, O., West, A.J., van Westen, C.J., Tanyas, H., Hovius, N., Hales, T.C., Jibson, R.W., Allstadt, K.E., Zhang, L., Evans, S.G., Xu, C., Li, G., Pei, X., Xu, Q., Huang, R., 2019. Earthquake-Induced Chains of Geologic Hazards: Patterns, Mechanisms, and Impacts. Rev. Geophys. https://doi.org/10.1029/2018RG000626

Fan, X., Xu, Q., van Westen, C.J., Huang, R., Tang, R., 2017. Characteristics and classification of landslide dams associated with the 2008 Wenchuan earthquake. Geoenvironmental Disasters 4. https://doi.org/10.1186/s40677-017-0079-8

Fourie, A.B., Blight, G.E., Papageorgiou, G., 2001. Static liquefaction as a possible explanation for the Merriespruit tailings dam failure. Can. Geotech. J. 38, 707–719. https://doi.org/10.1139/t00-112

Fukuzono, T., 1985. A Method to Predict the Time of Slope Failure Caused by Rainfall Using the Inverse Number of Velocity of Surface Displacement. J. Japan Landslide Soc. 22, 8-13_1. https://doi.org/10.3313/jls1964.22.2_8

Furuya, G., Sassa, K., Hiura, H., Fukuoka, H., 1999. Mechanism of creep movement caused by landslide activity and underground erosion in crystalline schist, Shikoku Island, southwestern Japan. Eng. Geol. 53, 311–325. https://doi.org/10.1016/S0013-7952(98)00084-2

Ge, Y., Zhou, T., Tang, H., Lin, Z., 2020. Influence of the impact angle on the motion and deposition of granular flows. Eng. Geol. 275, 105746. https://doi.org/10.1016/j.enggeo.2020.105746

Gratchev, I.B., Sassa, K., Osipov, V.I., Sokolov, V.N., 2006. The liquefaction of clayey soils under cyclic loading. Eng. Geol. 86, 70–84. https://doi.org/10.1016/j.enggeo.2006.04.006

Green, P.A., Ferguson, P.A.S., 1971. On Liquefaction Phenomena, by Professor A. Casagrande: Report of Lecture. Géotechnique 21, 197–202. https://doi.org/10.1680/geot.1971.21.3.197

HSÜ, K.J., 1975. Catastrophic Debris Streams (Sturzstroms) Generated by Rockfalls. GSA Bull. 86, 129–140. https://doi.org/10.1130/0016-7606(1975)86<129:Cdssgb>2.0.Co;2

Hu, W., Scaringi, G., Xu, Q., Huang, R., 2018. Internal Erosion Controls Failure and Runout of Loose Granular Deposits: Evidence From Flume Tests and Implications for Postseismic Slope Healing. Geophys. Res. Lett. 45, 5518–5527. https://doi.org/10.1029/2018GL078030

Hu, W., Scaringi, G., Xu, Q., Pei, Z., Van Asch, T.W.J., Hicher, P.-Y., 2017. Sensitivity of the initiation and runout of flowslides in loose granular deposits to the content of small particles: An insight from flume tests. Eng. Geol. 231, 34–44. https://doi.org/https://doi.org/10.1016/j.enggeo.2017.10.001

Huang, R., Pei, X., Fan, X., Zhang, W., Li, S., Li, B., 2011. The characteristics and failure mechanism of the largest landslide triggered by the Wenchuan earthquake, May 12, 2008, China. Landslides 9, 131–142. https://doi.org/10.1007/s10346-011-0276-6

Hutchinson, J.N., 1986. A sliding-consolidation model for flow slides. Can. Geotech. J. https://doi.org/10.1139/t86-021

Hutchinson, J.N., Bhandari, R.K., 1971. Undrained Loading, A Fundamental Mechanism of Mudflows

and other Mass Movements. Geotechnique. https://doi.org/10.1680/geot.1971.21.4.353
Intrieri, E., Gigli, G., Mugnai, F., Fanti, R., Casagli, N., 2012. Design and implementation of a landslide early warning system. Eng. Geol. https://doi.org/10.1016/j.enggeo.2012.07.017
Ishihara, K., 1993. Liquefaction and flow failure during earthquakes. Géotechnique 43, 351–451. https://doi.org/10.1680/geot.1993.43.3.351
Iverson, N.R., Mann, J.E., Iverson, R.M., 2010. Effects of soil aggregates on debris-flow mobilization: Results from ring-shear experiments. Eng. Geol. 114, 84–92. https://doi.org/https://doi.org/10.1016/j.enggeo.2010.04.006
Iverson, R.M., 2000. Acute Sensitivity of Landslide Rates to Initial Soil Porosity. Science (80-.). 290, 513–516. https://doi.org/10.1126/science.290.5491.513
Jurko, J., Sassa, K., Fukuoka, H., 2008. Study on seismic behavior of nonplastic silt by means of ring-shear apparatus. Landslides 5, 189. https://doi.org/10.1007/s10346-008-0113-8
Kanagalingam, T., Thevanayagam, S., 2005. Discussion: Contribution of fines to the compressive strength of mixed soils. Géotechnique 55, 627–628. https://doi.org/10.1680/geot.2005.55.8.627
Kluger, M.O., Moon, V.G., Kreiter, S., Lowe, D.J., Churchman, G.J., Hepp, D.A., Seibel, D., Jorat, M.E., Mörz, T., 2017. A new attraction-detachment model for explaining flow sliding in clay-rich tephras. Geology 45, 131–134. https://doi.org/10.1130/G38560.1
Krýza, O., Závada, P., Lexa, O., 2019. Advanced strain and mass transfer analysis in crustal-scale oroclinal buckling and detachment folding analogue models. Tectonophysics 764, 88–109. https://doi.org/10.1016/j.tecto.2019.05.001
Kwa, K.A., Airey, D.W., 2017. Effects of fines on liquefaction behaviour in well-graded materials. Can. Geotech. J. 54, 1460–1471. https://doi.org/10.1139/cgj-2017-0016
Lade, P. V., Liggio, C.D., Yamamuro, J.A., 1998. Effects of Non-Plastic Fines on Minimum and Maximum Void Ratios of Sand. Geotech. Test. J. https://doi.org/10.1520/gtj11373j
Li, K., Wang, Y.-F., Lin, Q.-W., Cheng, Q.-G., Wu, Y., 2021. Experiments on granular flow behavior and deposit characteristics: implications for rock avalanche kinematics. Landslides. https://doi.org/10.1007/s10346-020-01607-z
Li, Y., Hu, W., Wasowski, J., Zheng, Y., McSaveney, M., 2021. Rapid episodic erosion of a cohesionless landslide dam: Insights from loss to scour of Yangjia Gully check dams and from flume experiments. Eng. Geol. https://doi.org/10.1016/j.enggeo.2020.105971
Liao, H. mei, Yang, X. guo, Lu, G. da, Tao, J., Zhou, J. wen, 2019. Experimental study on the river blockage and landslide dam formation induced by rock slides. Eng. Geol. https://doi.org/10.1016/j.enggeo.2019.105269
McSaveney, M., Davies, T., 2007. Rockslides and Their Motion, in: Progress in Landslide Science. Springer Berlin Heidelberg, Berlin, Heidelberg, pp. 113–133. https://doi.org/10.1007/978-3-540-70965-7_8
McSaveney, M.J., Davies, T.R.H., 2006. Rapid Rock Mass Flow with Dynamic Fragmentation: Inferences from the Morphology and Internal Structure of Rockslides and Rock Avalanches, in: Landslides from Massive Rock Slope Failure. Springer Netherlands, Dordrecht, pp. 285–304. https://doi.org/10.1007/978-1-4020-4037-5_16
Mohammadi, A., Qadimi, A., 2015. A simple critical state approach to predicting the cyclic and monotonic response of sands with different fines contents using the equivalent intergranular void ratio. Acta Geotech. 10, 587–606. https://doi.org/10.1007/s11440-014-0318-z
Monkul, M.M., Etminan, E., Şenol, A., 2017. Coupled influence of content, gradation and shape

characteristics of silts on static liquefaction of loose silty sands. Soil Dyn. Earthq. Eng. 101, 12–26. https://doi.org/10.1016/j.soildyn.2017.06.023

Monkul, M.M., Yamamuro, J.A., 2011. Influence of silt size and content on liquefaction behavior of sands. Can. Geotech. J. 48, 931–942. https://doi.org/10.1139/t11-001

Moriwaki, H., Inokuchi, T., Hattanji, T., Sassa, K., Ochiai, H., Wang, G., 2004. Failure processes in a full-scale landslide experiment using a rainfall simulator. Landslides 1, 277–288. https://doi.org/10.1007/s10346-004-0034-0

Murthy, T.G., Loukidis, D., Carraro, J.A.H., Prezzi, M., Salgado, R., 2007. Undrained monotonic response of clean and silty sands. Géotechnique 57, 273–288. https://doi.org/10.1680/geot.2007.57.3.273

Ni, Q., Tan, T.S., Dasari, G.R., Hight, D.W., 2004. Contribution of fines to the compressive strength of mixed soils. Géotechnique 54, 561–569. https://doi.org/10.1680/geot.2004.54.9.561

Ochiai, H., Okada, Y., Furuya, G., Okura, Y., Matsui, T., Sammori, T., Terajima, T., Sassa, K., 2004. A fluidized landslide on a natural slope by artificial rainfall. Landslides 1, 211–219. https://doi.org/10.1007/s10346-004-0030-4

Okura, Y., Kitahara, H., Ochiai, H., Sammori, T., Kawanami, A., 2002. Landslide fluidization process by flume experiments. Eng. Geol. 66, 65–78. https://doi.org/https://doi.org/10.1016/S0013-7952(02)00032-7

Olivares, L., Damiano, E., 2007. Postfailure Mechanics of Landslides: Laboratory Investigation of Flowslides in Pyroclastic Soils. J. Geotech. Geoenvironmental Eng. 133, 51–62. https://doi.org/10.1061/(asce)1090-0241(2007)133:1(51)

Ouyang, C., Zhou, K., Xu, Q., Yin, J., Peng, D., Wang, D., Li, W., 2017. Dynamic analysis and numerical modeling of the 2015 catastrophic landslide of the construction waste landfill at Guangming, Shenzhen, China. Landslides. https://doi.org/10.1007/s10346-016-0764-9

Papadopoulou, A., Tika, T., 2008. The Effect of Fines on Critical State and Liquefaction Resistance Characteristics of Non-Plastic Silty Sands. Soils Found. 48, 713–725. https://doi.org/10.3208/sandf.48.713

Peng, J., Zhuang, J., Wang, G., Dai, F., Zhang, F., Huang, W., Xu, Q., 2018. Liquefaction of loess landslides as a consequence of irrigation. Q. J. Eng. Geol. Hydrogeol. https://doi.org/10.1144/qjegh2017-098

Perinotto, H., Schneider, J.-L., Bachèlery, P., Le Bourdonnec, F.-X., Famin, V., Michon, L., 2015. The extreme mobility of debris avalanches: A new model of transport mechanism. J. Geophys. Res. Solid Earth 120, 8110–8119. https://doi.org/10.1002/2015jb011994

Pitman, T.D., Robertson, P.K., Sego, D.C., 1994. Influence of fines on the collapse of loose sands. Can. Geotech. J. 31, 728–739. https://doi.org/10.1139/t94-084

Polito, C.P., Martin II, J.R., 2001. Effects of Nonplastic Fines on the Liquefaction Resistance of Sands. J. Geotech. Geoenvironmental Eng. 127, 408–415. https://doi.org/10.1061/(ASCE)1090-0241(2001)127:5(408)

Porcino, D.D., Diano, V., 2017. The influence of non-plastic fines on pore water pressure generation and undrained shear strength of sand-silt mixtures. Soil Dyn. Earthq. Eng. 101, 311–321. https://doi.org/10.1016/j.soildyn.2017.07.015

Porcino, D.D., Triantafyllidis, T., Wichtmann, T., Tomasello, G., 2021. Application of Critical State Approach to Liquefaction Resistance of Sand–Silt Mixtures under Cyclic Simple Shear Loading. J. Geotech. Geoenvironmental Eng. 147, 04020177. https://doi.org/10.1061/(ASCE)GT.1943-

5606.0002470

Qi, C., Zheng, J., Zuo, D., Chen, G., 2017. Measurement on soil deformation caused by expanded-base pile in transparent soil using particle image velocimetry (PIV). J. Mt. Sci. 14, 1655–1665. https://doi.org/10.1007/s11629-016-4025-0

Qi, X., Xu, Q., Liu, F., 2018. Analysis of retrogressive loess flowslides in Heifangtai, China. Eng. Geol. 236, 119–128. https://doi.org/10.1016/j.enggeo.2017.08.028

Rahman, M.M., Lo, S.R., 2008. The prediction of equivalent granular steady state line of loose sand with fines. Geomech. Geoengin. 3, 179–190. https://doi.org/10.1080/17486020802206867

Rahman, M.M., Lo, S.R., Baki, M.A.L., 2011. Equivalent granular state parameter and undrained behaviour of sand-fines mixtures. Acta Geotech. 6, 183–194. https://doi.org/10.1007/s11440-011-0145-4

Rahman, M.M., Lo, S.R., Gnanendran, C.T., 2009. Reply to the discussion by wanatowski and chu on "on equivalent granular void ratio and steady state behaviour of loose sand with fines." Can. Geotech. J. 46, 483–486. https://doi.org/10.1139/T09-025

Rahman, M.M., Lo, S.R., Gnanendran, C.T., 2008. On equivalent granular void ratio and steady state behaviour of loose sand with fines. Can. Geotech. J. 45, 1439–1456. https://doi.org/10.1139/t08-064

Rahman, M.M., Sitharam, T.G., 2020. Cyclic liquefaction screening of sand with non-plastic fines: Critical state approach. Geosci. Front. 11, 429–438. https://doi.org/10.1016/j.gsf.2018.09.009

Rahmani, H., Abolhasan Naeini, S., 2020. Influence of non-plastic fine on static iquefaction and undrained monotonic behavior of sandy gravel. Eng. Geol. 275, 105729. https://doi.org/10.1016/j.enggeo.2020.105729

Sabbar, A.S., Chegenizadeh, A., Nikraz, H., 2017. Static liquefaction of very loose sand–slag–bentonite mixtures. SOILS Found. 57, 341–356. https://doi.org/10.1016/j.sandf.2017.05.003

Saito, R., Sassa, K., Fukuoka, H., 2007. Effects of shear rate on the internal friction angle of silica sand and bentonite mixture samples. J. Japan Landslide Soc. https://doi.org/10.3313/jls.44.33

Sarno, L., Carravetta, A., Tai, Y.-C., Martino, R., Papa, M.N., Kuo, C.-Y., 2018. Measuring the velocity fields of granular flows – Employment of a multi-pass two-dimensional particle image velocimetry (2D-PIV) approach. Adv. Powder Technol. 29, 3107–3123. https://doi.org/10.1016/j.apt.2018.08.014

Sassa, K., 1998. Mechanisms of Landslide Triggered Debris Flows, in: Sassa, K. (Ed.), Environmental Forest Science: Proceedings of the IUFRO Division 8 Conference Environmental Forest Science, Held 19–23 October 1998, Kyoto University, Japan. Springer Netherlands, Dordrecht, pp. 499–518. https://doi.org/10.1007/978-94-011-5324-9_53

Sassa, K., 1988. Geotechnical model for the motion of landslides (Special lecture). Proceedings, 5th Int'l. Symp. Landslides. Lausanne 1, 37–56.

Sassa, K., Fukuoka, H., Scarascia-Mugnozza, G., Evans, S., 1996. EARTHQUAKE-INDUCED-LANDSLIDES : DISTRIBUTION, MOTION AND MECHANISMS. SOILS Found. 36, 53–64. https://doi.org/10.3208/sandf.36.Special_53

Seed, H.B., 1979. Soil Liquefaction and Cyclic Mobility Evaluation for Level Ground during Earthquakes. J. Geotech. Eng. Div. 105, 201–255. https://doi.org/10.1061/AJGEB6.0000768

Seed, H.B., 1968. Landslides during earthquakes due to liquefaction. J. Smfe Proc Asce 94, 1055–1122.

Siman-Tov, S., Brodsky, E.E., 2018. Gravity-Independent Grain Size Segregation in Experimental

Granular Shear Flows as a Mechanism of Layer Formation. Geophys. Res. Lett. 45, 8136–8144. https://doi.org/10.1029/2018gl078486

Smethurst, J.A., Smith, A., Uhlemann, S., Wooff, C., Chambers, J., Hughes, P., Lenart, S., Saroglou, H., Springman, S.M., Löfroth, H., Hughes, D., 2017. Current and future role of instrumentation and monitoring in the performance of transport infrastructure slopes. Q. J. Eng. Geol. Hydrogeol. https://doi.org/10.1144/qjegh2016-080

Spence, K.J., Guymer, I., 1997. Small-scale laboratory flowslides. Géotechnique 47, 915–932. https://doi.org/10.1680/geot.1997.47.5.915

Stanier, S.A., Blaber, J., Take, W.A., White, D.J., 2016. Improved image-based deformation measurement for geotechnical applications. Can. Geotech. J. https://doi.org/10.1139/cgj-2015-0253

Stanier, S.A., White, D.J., 2013. Improved image-based deformation measurement in the centrifuge environment. Geotech. Test. J. https://doi.org/10.1520/GTJ20130044

Take, W.A., Beddoe, R.A., Davoodi-Bilesavar, R., Phillips, R., 2014. Effect of antecedent groundwater conditions on the triggering of static liquefaction landslides. Landslides 12, 469–479. https://doi.org/10.1007/s10346-014-0496-7

Take, W.A., Bolton, M.D., Wong, P.C.P., Yeung, F.J., 2004. Evaluation of landslide triggering mechanisms in model fill slopes. Landslides. https://doi.org/10.1007/s10346-004-0025-1

Tang, J., Taro, U., Huang, D., Xie, J., Tao, S., 2020. Physical Model Experiments on Water Infiltration and Failure Modes in Multi-Layered Slopes under Heavy Rainfall. Appl. Sci. 10. https://doi.org/10.3390/app10103458

Taylor, S.E., Brodsky, E.E., 2020. Reversible Compaction in Sheared Granular Flows and Its Significance for Nonlocal Rheology. Geophys. Res. Lett. 47. https://doi.org/10.1029/2020gl087137

Teng, Y., Stanier, S.A., Gourvenec, S.M., 2020. Mechanisms beneath rectangular shallow foundations on sands: Vertical loading. Geotechnique. https://doi.org/10.1680/jgeot.18.P.058

Thevanayagam, S., 2007a. Intergrain contact density indices for granular mixes—II: Liquefaction resistance. Earthq. Eng. Eng. Vib. 6, 135–146. https://doi.org/10.1007/s11803-007-0706-6

Thevanayagam, S., 2007b. Intergrain contact density indices for granular mixes—I: Framework. Earthq. Eng. Eng. Vib. 6, 123–134. https://doi.org/10.1007/s11803-007-0705-7

Thevanayagam, S., 1998. Effect of Fines and Confining Stress on Undrained Shear Strength of Silty Sands. J. Geotech. Geoenvironmental Eng. 124, 479–491. https://doi.org/10.1061/(ASCE)1090-0241(1998)124:6(479)

Thevanayagam, S., Mohan, S., 2000. Intergranular state variables and stress–strain behaviour of silty sands. Géotechnique 50, 1–23. https://doi.org/10.1680/geot.2000.50.1.1

Thevanayagam, S., Shenthan, T., Mohan, S., Liang, J., 2002. Undrained Fragility of Clean Sands, Silty Sands, and Sandy Silts. J. Geotech. Geoenvironmental Eng. 128, 849–859. https://doi.org/doi:10.1061/(ASCE)1090-0241(2002)128:10(849)

Thielicke, W., Stamhuis, E.J., 2014. PIVlab – Towards User-friendly, Affordable and Accurate Digital Particle Image Velocimetry in MATLAB. J. Open Res. Softw. 2. https://doi.org/10.5334/jors.bl

Tsuchida, T., Kano, S., Nakagawa, S., Kaibori, M., Nakai, S., Kitayama, N., 2014. Landslide and mudflow disaster in disposal site of surplus soil at Higashi-Hiroshima due to heavy rainfall in 2009. Soils Found. 54, 621–638. https://doi.org/10.1016/j.sandf.2014.06.005

Uchimura, T., Towhata, I., Anh, T.T.L., Fukuda, J., Bautista, C.J.B., Wang, L., Seko, I., Uchida, T.,

Matsuoka, A., Ito, Y., Onda, Y., Iwagami, S., Kim, M.S., Sakai, N., 2010. Simple monitoring method for precaution of landslides watching tilting and water contents on slopes surface. Landslides. https://doi.org/10.1007/s10346-009-0178-z

Uchimura, T., Towhata, I., Wang, L., Nishie, S., Yamaguchi, H., Seko, I., Qiao, J., 2015. Precaution and early warning of surface failure of slopes using tilt sensors. Soils Found. https://doi.org/10.1016/j.sandf.2015.09.010

Wang, F., Wu, Y.-H., Yang, H., Tanida, Y., Kamei, A., 2015. Preliminary investigation of the 20 August 2014 debris flows triggered by a severe rainstorm in Hiroshima City, Japan. Geoenvironmental Disasters 2, 17. https://doi.org/10.1186/s40677-015-0025-6

Wang, G., Sassa, K., 2003. Pore-pressure generation and movement of rainfall-induced landslides: effects of grain size and fine-particle content. Eng. Geol. 69, 109–125. https://doi.org/10.1016/s0013-7952(02)00268-5

Wang, G., Sassa, K., 2001. Factors affecting rainfall-induced flowslides in laboratory flume tests. Géotechnique 51, 587–599. https://doi.org/10.1680/geot.2001.51.7.587

Wang, G., Sassa, K., 1998. An Experimental Study on the Rainfall-Induced-Flowslides, in: Sassa, K. (Ed.), Environmental Forest Science: Proceedings of the IUFRO Division 8 Conference Environmental Forest Science, Held 19–23 October 1998, Kyoto University, Japan. Springer Netherlands, Dordrecht, pp. 591–598. https://doi.org/10.1007/978-94-011-5324-9_62

Wang, G., Sassa, K., Fukuoka, H., 2003. Downslope volume enlargement of a debris slide–debris flow in the 1999 Hiroshima, Japan, rainstorm. Eng. Geol. 69, 309–330. https://doi.org/https://doi.org/10.1016/S0013-7952(02)00289-2

Wang, G., Suemine, A., Furuya, G., Kaibori, M., Sassa, K., 2005. Rainstorm-induced landslides at Kisawa village, Tokushima Prefecture, Japan, August 2004. Landslides 2, 235–242. https://doi.org/10.1007/s10346-005-0061-5

Wasowski, J., McSaveney, M.J., Pisano, L., Del Gaudio, V., Li, Y., Hu, W., 2021. Recurrent rock avalanches progressively dismantle a mountain ridge in Beichuan County, Sichuan, most recently in the 2008 Wenchuan earthquake. Geomorphology. https://doi.org/10.1016/j.geomorph.2020.107492

Wei, L., Xu, Q., Wang, S., Wang, C., Ji, X., 2020. The morphology evolution of the shear band in slope: insights from physical modelling using transparent soil. Bull. Eng. Geol. Environ. 79, 1849–1860. https://doi.org/10.1007/s10064-019-01649-1

Xie, J., Uchimura, T., Wang, G., Selvarajah, H., Maqsood, Z., Shen, Q., Mei, G., Qiao, S., 2020. Predicting the sliding behavior of rotational landslides based on the tilting measurement of the slope surface. Eng. Geol. https://doi.org/10.1016/j.enggeo.2020.105554

Xu, Q., Peng, D., Zhang, S., Zhu, X., He, C., Qi, X., Zhao, K., Xiu, D., Ju, N., 2020. Successful implementations of a real-time and intelligent early warning system for loess landslides on the Heifangtai terrace, China. Eng. Geol. https://doi.org/10.1016/j.enggeo.2020.105817

Yamamuro, J.A., Lade, P. V, 1997. Static liquefaction of very loose sands. Can. Geotech. J. 34, 905–917. https://doi.org/10.1139/t97-057

Yang, J., Wei, L.M., 2012. Collapse of loose sand with the addition of fines: the role of particle shape. Géotechnique 62, 1111–1125. https://doi.org/10.1680/geot.11.P.062

Yin, Y., Xing, A., Wang, G., Feng, Z., Li, B., Jiang, Y., 2016. Experimental and numerical investigations of a catastrophic long-runout landslide in Zhenxiong, Yunnan, southwestern China. Landslides 14, 649–659. https://doi.org/10.1007/s10346-016-0729-z

Zhang, F., Kang, C., Chan, D., Zhang, X., Pei, X., Peng, J., 2017. A study of a flowslide with significant entrainment in loess areas in China. Earth Surf. Process. Landforms. https://doi.org/10.1002/esp.4184

Zhang, S., Zhang, L.M., 2017. Impact of the 2008 Wenchuan earthquake in China on subsequent long-term debris flow activities in the epicentral area. Geomorphology 276, 86–103. https://doi.org/10.1016/j.geomorph.2016.10.009

Zhang, X., Hu, W., Zheng, Y., Gou, H., Gao, X., 2020. Effects of Relative Density in Progressive Sliding of Tailings deposits: Insights from Flume Tests. Eng. Geol. 279, 105908. https://doi.org/10.1016/j.enggeo.2020.105908

Zuo, L., Baudet, B.A., 2020. Normalised behaviour of a non-plastic silt–pumice sand mixture. Géotechnique 70, 822–832. https://doi.org/10.1680/jgeot.19.P.012

Zuo, L., Baudet, B.A., 2015. Determination of the transitional fines content of sand-non plastic fines mixtures. Soils Found. 55, 213–219. https://doi.org/10.1016/j.sandf.2014.12.017